

# Dynamics of collisionless rf plasma sheaths

Paul A. Miller<sup>a)</sup> and Merle E. Riley

Sandia National Laboratories, Box 5800, Albuquerque, New Mexico 87185-1423

(Received 4 April 1997; accepted for publication 14 July 1997)

The behavior of rf plasma sheaths has been the subject of much scientific study and also is technologically important for plasma etching and deposition in the manufacture of integrated circuits. This paper presents a semianalytic model of rf sheaths and describes an experiment that tested the model. An approximation to the first integral of the Poisson equation allows solving for the response of plasma sheaths to an imposed rf bias voltage. This approximation enables the plasma sheaths to be included within an electrical model of the plasma and external rf circuit components, and affords a prediction of the ion energy distributions impacting the electrodes, which are in contact with the plasma. The model is a significant advance beyond previous sheath models because it has no restriction on the ratio of the rf period to the ion transit time across the sheath. The model is applicable to those high-density, low-pressure plasmas in which the Debye length is a small fraction of the ion mean-free path, which itself is a small fraction of the plasma dimension. The experimental test of the model was conducted by comparing the predicted and measured rf potential, current, and power at the sheath adjacent to a capacitively coupled, rf-biased electrode in a plasma reactor with argon discharges sustained by an inductively coupled plasma source. The comparisons included both linear and nonlinear components of the rf electrical parameters. Results of the experiment were in substantial agreement with model predictions. © 1997 American Institute of Physics. [S0021-8979(97)06320-2]

## I. INTRODUCTION

The behavior of plasma sheaths has been a topic of much scientific interest for decades, and also is of great technological importance. For example, in the manufacture of integrated circuits, it is common to use rf-excited plasmas for etching and deposition of a variety of materials. Source gases injected into plasma chambers undergo a variety of electrical and chemical reactions in the bulk plasma, and the resulting reactive species, charged and neutral, are extracted onto the work piece through a plasma sheath close to the work piece. Uncharged species flow freely across the sheath, while charged species may be accelerated or decelerated by sheath potentials. The physics of the plasma sheath is the specific focus of the work reported here. Our goal is to understand more about the electrodynamics of the sheath and the external electrical manifestations of the sheath behavior.

The work reported here emphasizes so-called “high-density” plasmas used in the microelectronics industry for etching of semiconductor wafers. Typical parameters in the bulk of plasmas of interest are electron and ion densities of  $10^{10}$ – $10^{12}/\text{cm}^3$ , electron temperatures of a few or several electron volts, and gas pressures below 20 mTorr. Resulting plasma screening lengths are a fraction of a millimeter and, consequently, the sheaths may be treated as collisionless. We study sheaths that have both ac and dc potentials imposed across them. The electrons in the plasma are assumed to be in thermal equilibrium with the local plasma potential (Boltzmann distribution) and, thus, electron inertial effects are not treated. This restricts the applicability of the analysis to the frequency range from dc through VHF. Our experiments, which were compared to the theory, involved dc potentials

and ac potentials at 13.56 MHz (and harmonics thereof) appearing across the plasma sheaths.

Because we focus our attention on the electrodynamics of the plasma sheath, the bulk of the plasma is treated as a boundary condition of the sheath problem. In general, net power flows through the plasma sheath, which can affect the properties of the bulk plasma. In the case of capacitively excited discharges, the power flowing through the sheath is the entire source of power that sustains the discharge. In industrial “high-density” plasma reactors, separate power sources are usually used to provide power to the bulk of the plasma and to power the sheath at the work piece. The nature of the source that generates the bulk plasma is not relevant to the present study, only the resulting values of plasma density and temperature are important. While our experiments employed an inductively coupled rf source based on systems developed previously by others<sup>1–9</sup> to sustain the bulk plasma, the work would be equally applicable to plasmas sustained, for example, by electron–cyclotron–resonance heating or by microwave heating. The mechanism of the bulk-plasma-generation process is not addressed here.

The sheath model and the experiment reported here directly address the sheath adjacent to the rf-biased electrode in an inductively coupled plasma reactor, similar to those used for processing of wafers in the microelectronics industry. That biased electrode, sometimes called the cathode or chuck, was coupled through a dc blocking capacitor to a source of rf power. Inasmuch as the rf bias power flowed through the sheath at the biased electrode, through the bulk plasma, and to the reactor walls, the system model reported here necessarily included treatments of the sheaths at all of the reactor’s walls and a limited treatment of the bulk plasma. Section II discusses the parts of the bulk plasma, mainly the plasma potential, that were addressed in detail in

<sup>a)</sup>Electronic mail: pamille@sandia.gov

this work. Section III presents the detailed derivation of the analytic sheath model and Sec. IV discusses why and how the sheath model was connected to an rf-circuit model. Section V describes experimental hardware and techniques, and includes subsections describing the laboratory reactor; rf-power circuits; measurement of the rf potential, current, and impedance; and use of capacitive and Langmuir probes. Section VI presents comparisons of experimental measurements and model predictions. Section VII describes model predictions that demonstrate the sensitivity of the energy-distribution function of ions to details of the rf circuit that provides the rf power to the electrode. Section VIII summarizes the work.

## II. BULK PLASMA TREATMENT

A comprehensive model for a plasma reactor must treat the bulk plasma as well as plasma sheaths. Recently, many workers have explored with success a variety of approaches in developing bulk-plasma models suitable for describing high-density plasma reactors.<sup>10–16</sup> In general, it is computationally challenging to describe both the sheaths and the bulk in a single model because of the diverse scale lengths and time constants involved in the bulk and the sheaths. The modeling work described here emphasized only the behavior of the plasma sheaths and did not include detailed modeling of the bulk plasma. The plasma-sheath model (Sec. III) requires as input the bulk-plasma parameters at the “edge” of the plasma sheath. Those parameters are the plasma electron temperature  $T_e$ , the electron density  $n_e$ , and the ion mass  $m$ . We used values measured in the experiment for  $T_e$  and  $n_e$  instead of values from a bulk model. Because of spatial variations in  $T_e$ ,  $n_e$ , and in the plasma potential  $V_p$ , there is a subtle issue regarding  $V_p$  in performing the calculations. That issue does not have a major impact on the results of the calculations, but, for completeness, we describe it in detail.

The reactor geometry in this work had the inductive plasma source at the top of the reactor and the planar, capacitively coupled electrode at the bottom. The rf-biased lower electrode corresponded to the wafer chuck in an industrial reactor. The model calculations were started with quiescent conditions, i.e., without applied rf drive on the lower electrode of the reactor. Subsequently, the rf bias in the model was ramped over many cycles (typically, 10–100) to reach a steady-state condition with the applied rf bias. Under the initial quiescent conditions, the lower electrode of the reactor had no net dc current to it because there was a dc-blocking capacitor connecting it to the rf-bias power supply. Consequently, there also was no net dc current to the reactor walls. However, our sheath model does allow eddy currents, i.e., a current could flow to one part of an electrode, as long it was balanced by an equal flow away from another part of that same electrode. Such flows would be caused by spatial variations in  $V_p$  and  $T_e$  that did not give zero net current to every small part of a single electrode.

Because the sheath model assumed a Maxwellian distribution of electrons, the specifications of  $T_e$  and  $m$ , along with current flows and wall potentials, were sufficient to determine uniquely the local value of plasma potential  $V_p$  in the model. In the experiment, we used a Langmuir probe to

determine  $n_e$ ,  $T_e$ , and  $V_p$ . Those values were measured as functions of position near the walls of the reactor and used as boundary conditions for the model. Either due to measurement error or due to non-Maxwellian distributions, the measured values of  $T_e$  and  $V_p$ , under quiescent conditions, were not always precisely consistent with zero net dc currents to the lower electrode and to the walls in the model. Adjustments of some kind were required in order to allow the computation to be initialized self-consistently with zero net currents. In treating the lower electrode in the calculations, we assumed that the measured values of  $T_e$  and  $V_p$ , which varied across the electrode, were exactly correct. We then adjusted the floating potential of the lower electrode  $V_f$  in the code to give zero net current to that electrode. The computed and measured values of  $V_f$  were always close to 0 V and within 2 V of each other. In treating the plasma near the grounded chamber walls, we assumed that the measured values of  $T_e$  were exactly correct. We then shifted all the plasma potentials adjacent to the walls in the calculation up or down uniformly from the measured values in order to achieve zero net current to the walls. The required potential shift was always less than 2 V. These shifts in  $V_f$  and in  $V_p$  were small compared to typical values of  $V_p$ , which ranged from 15 to 21 V. It is a historical accident that the potential adjustments at the walls and lower electrode were performed differently. We could have adjusted  $V_p$  at the lower electrode and held  $V_f$  fixed, and the results should have been the same.

To summarize the initial conditions of the calculations: (1) The calculations used the spatially varying values of  $n_e$  and  $T_e$  as measured by Langmuir probe. (2) The calculations used the measured plasma potentials near the lower electrode. (3) The potential of the lower electrode in the calculations was shifted by  $<2$  V from the measured value to give zero net current to the electrode. (4) The plasma potentials near the chamber walls were all shifted from the measured values by an amount ( $<2$  V) needed to give zero net current to the walls.

When rf bias was applied, the average value of the plasma potentials changed and the plasma potentials became modulated at the bias frequency (plus harmonics). The bulk plasma was assumed to have very high conductivity at the rf frequencies in this work. Consequently, the modulation of  $V_p$  in the model was forced to be the same in amplitude and phase throughout the bulk plasma, and thus, identical rf modulation of the potential appeared across all sheaths. The calculations also assumed that the shift in the average value (the dc component) of  $V_p$  changed by the same amount throughout the plasma. These assumptions were tested and found to be fairly accurate in our reactor, as described below in Sec. VI A. This modeling of the plasma potential meant that no bias power could be dissipated in the bulk plasma, and thus, the bias power could not affect the bulk-plasma properties or the uniformity of the ion flux to the lower electrode. This differs from the results of Grapperhaus and Kushner.<sup>17</sup> Their model included a self-consistent treatment of the bulk plasma with a sheath model and they found a moderate dependence of ion uniformity on rf bias power. The magnitude of this discrepancy may be a function of

parameters such as reactor size, and this subject is worthy of further investigation.

### III. PLASMA SHEATH MODEL

In this section, we develop a model of the plasma sheath that is applicable to low-pressure, high-density plasmas. The sheath is assumed to be perturbed by an applied rf bias potential that controls the ion energies that fall through the sheath. The sheath model does not apply to plasmas in which the amplitude of the sheath motion is on the order of the bulk plasma dimension.

Lieberman's<sup>18</sup> theory of a rf-driven plasma sheath leads to an analytic solution for the anharmonic voltage required to produce a prescribed sinusoidal rf displacement current due to electron motion. The model assumes that the electron density is equal to the ion density inside the sharp electron boundary, and is zero towards the electrode. This sharp boundary is a low-electron-temperature approximation, and is a unique feature of the Lieberman model. There is no electron particle current to the electrode, and the ion current to the electrode is constant and monoenergetic. The rf current, which is a displacement current, is due to the oscillation of the electron boundary within the sheath. The time-independent ion density distribution within the sheath is computed self-consistently, assuming that the ions see only the time average of the potential. In other words, the ions are completely inertial and monoenergetic, responding only to the average field. The limitations of this model for our application are mainly due to a lack of electron particle current to the wall, the requirement of sinusoidal current, and the restriction to the inertial-ion case (high-frequency limit).

Another model for a rf plasma sheath is that of Metze, Ernie, and Oskam<sup>19</sup> (MEO), which assumes that the electrons and the ions both respond instantaneously to an imposed time variation of the sheath potential (low-frequency limit). The MEO model is a quasi-steady-state (QSS) model of the particle dynamics in which the ions, as well as the electrons, effectively have no inertia. This model includes electron particle current to the wall, as well as ion current and displacement current. This model becomes accurate as the frequency of the applied field becomes much less than the ion plasma frequency.

A unified model that connects these two limiting theories would be of importance in the simulation of plasma sheath dynamics because many cases of interest are not well described by the limits of the previous models. Such a unified model has been developed by one of the authors in a pair of technical reports,<sup>20,21</sup> and appears to be fairly robust. It is described in this section. The model is a generalization of the QSS model, with ion inertia added into the theory by means of an approximate first integral of the Poisson equation and a time damping procedure for simulation of the ion response. The sheath can treat plasmas containing multiple ion species, although the experiment described below involved only a single ion species.

The recent study by Grapperhaus and Kushner,<sup>17</sup> in which they used the unified sheath model in the hybrid equipment model for plasma processing reactors, illustrates

the importance of including sheath effects in reactor-scale simulations.

#### A. Basic foundations of the plasma model

##### 1. The equations of motion of the plasma

In this section, we give the equations of motion (EOM), which we apply to the low-pressure, high-density plasmas of interest.<sup>22–25</sup> We assume that these EOM are globally valid from the bulk to the walls. The reason we consider the bulk region is because the plasma-sheath model needs boundary conditions for the ions that enter the sheath. Only by considering the whole plasma can we arrive at boundary conditions for the sheath model itself. Once we have developed the boundary conditions, the plasma sheath can be studied in isolation.

Consider a plasma in contact with material walls or electrodes. In the vicinity of a wall, the plasma is effectively one-dimensional, which greatly simplifies the EOM we use to describe the plasma sheath. The spatial coordinate is along the local outwardly directed normal to the wall. The major charged particles in the plasma are assumed to be one or more singly charged positive ion species and electrons, of number densities  $n_i$  and  $n_e$ . Negative ions, if present, are usually confined to the plasma bulk and do not enter into the sheath dynamics. Our only concern about negative ions is that the electron density must be a large-enough fraction of the negative charge within the plasma in order for the Boltzmann-electron and ambipolar assumptions to hold. The plasma ions are described by the fluid continuity equation

$$\dot{n}_i + (n_i u_i)' = r_i, \quad (1)$$

where  $u_i$  is the ion fluid velocity, and  $r_i$  is the volume ionization source rate for species  $i$ , and by the momentum equation,

$$\dot{u}_i + u_i u_i' = \frac{e}{m_i} E - \nu_i u_i, \quad (2)$$

where  $E = -\phi'$  is the electric field,  $\nu_i$  is the collision frequency of the ion, and the ion diffusion term has been neglected. Ion thermal diffusion is dominated by ambipolar diffusion in the bulk, and it is unimportant in the sheath transition region. There is a constant background neutral density  $N_0$ , which is, typically, considerably larger than the plasma electron and ion densities. The collision frequency is related to the background density, ion velocity, and an ion-neutral scattering cross section

$$\nu_i = N_0 v_i \sigma_i. \quad (3)$$

The velocity  $v_i$  in this relation will be approximated as the ion fluid velocity. This is not precisely correct,<sup>26</sup> but the error is not great, provided that the drift velocity of the ions is greater than the thermal velocities of the ions and background gas. This restricts the validity of Eq. (3) to the sheath and presheath regions.

The electrons are assumed to be in an equilibrium distribution at temperature  $T_e$  in the plasma. This is reasonable because of the electron's mean energy (a few eV) and light mass, the high plasma density, and the low pressure, all of

which contribute to the rapid establishment of thermal equilibrium among the electrons. We do not account for electron inertia, which is unimportant throughout the rf range of interest, at least once the means of energy input to the plasma and the ionization rate are specified. In other words, the electrons obey the quasi-steady-state Boltzmann distribution in the potential field. This relation can be expressed in either differential form or in integral form using values at some reference point  $x_0$  within the plasma,

$$\begin{aligned} n_e'/n_e &= e\phi'/kT_e, \\ n_e &= n_0 \exp[e(\phi - \phi_0)/kT_e], \end{aligned} \quad (4)$$

where  $\phi$  is the potential. The differential form of the Boltzmann distribution in Eq. (4) may be obtained directly by equating the large electron mobility and diffusion terms in the drift-diffusion approximation to the electron fluid momentum equation (not shown). This is an argument that may be used to derive the equilibrium distribution of the electrons. We have neglected the highly nonthermal secondary electrons returning to the bulk, which are produced by ion impact on the wall. These secondaries could add as much as 30% (due to a typical 0.3 electron yield per ion on metals) to the net current, but their effect on the charge balance within the sheath is negligible. In the absence of any good scheme for treating these electrons, we neglect them. Later, in Sec. VI B, we will discuss studies which we believe show that the precise shape of the electron distribution function is not too important.

Poisson's equation describes the collective interaction of the charged species

$$\phi'' = -\frac{e}{\epsilon_0} \left( \sum_i n_i - n_e \right). \quad (5)$$

All other symbols are as usually defined. Equations (1)–(5) constitute the basic starting EOM for the development of the sheath model.

## 2. Scaling relations within the plasma

A useful approach is to scale the EOM so that redundant information is removed. The potential (and electric field,  $E = -\phi'$ ) is scaled with the presumed constant electron temperature. We also use the reference value  $\phi_0$  for the potential that was introduced in Eq. (4),

$$\begin{aligned} \chi &= e(\phi - \phi_0)/kT_e, \\ \chi' &= e\phi'/kT_e. \end{aligned} \quad (6)$$

$\chi$  is dimensionless and  $\chi'$  is of dimension inverse length.

The ion mean free path,  $\lambda_i$ , is a convenient and mathematically useful scaling for the space coordinate if all ion mean-free paths are about the same. This, indeed, can be the case. Even if the  $\lambda_i$  are not all the same, the plasma is frequently dominated by a single ion species, as is the experimental study at hand. Consider different singly charged positive ions scattering from a background neutral gas. The momentum transfer cross section for classical charge-induced dipole scattering depends on the ion identity only through an inverse square root of the ion's kinetic energy,<sup>26</sup>

$$\begin{aligned} \sigma_i(E_i) &= \sigma(E_i) \approx 2\pi\sqrt{C/E_i}, \\ E_i &= \frac{1}{2}m_i v_i^2. \end{aligned} \quad (7)$$

This is appropriate for an ion energy above the neutral background gas thermal energy.  $C$  is the interaction constant depending on the polarizability of the background gas. For ion-neutral momentum transfer due to elastic scattering, the product of  $v\sigma(v)$  is nearly constant due to the ‘‘Maxwell molecule’’ effect for  $1/r^4$  interactions. Different species of drifting, singly charged positive ions with cross sections depending on their energy, all have the *same* mean energy if the mean ion velocity is assumed to be close to the drift velocity,

$$\begin{aligned} v_i &= N_0 v_i \sigma_i \equiv v_i / \lambda_i, \\ \lambda_i &= 1/N_0 \sigma_i, \\ v_i &\approx u_i = \mu_i E, \\ \mu_i &= e/m_i v_i. \end{aligned} \quad (8)$$

$\mu_i$  is the mobility of ion  $i$ . The solution to Eqs. (7) and (8) for the ion energy in the case of the charge-induced dipole scattering law is just

$$E_i \approx (eE/4\pi N_0)^2 / C \quad (9)$$

where  $C$  is the interaction constant in Eq. (7). Resonant charge exchange of an ion with its parent neutral could invalidate this argument, but we are using it only to set certain boundary conditions for the sheath model with multiple ions. At the extreme, the multiple ions could be replaced by one ‘‘average’’ ion.

The common energy means that all the ion species would have about the same mean free path:

$$1/\lambda_i = N_0 \sigma_i(E_i) \approx N_0 \sigma(E_i) \approx N_0 \sigma(E) = 1/\lambda. \quad (10)$$

The mean-free-path  $\lambda$  can be used for distance scaling in the EOM. The fact that  $\lambda$  is position dependent because of its dependence on ion energy does not seriously affect the argument. Time cannot be given a common scaling for all the ions by this argument. One notes that the characteristic time for ion motion might be the time between collisions of a few eV ‘‘average’’ ion.

Another coordinate characteristic length to be introduced is the Debye length  $\lambda_0$  characteristic of the plasma electron density  $n_0$  at reference point  $x_0$ , as introduced in Eq. (4),

$$\lambda_0^2 = \epsilon_0 kT_e / e^2 n_0. \quad (11)$$

Combine Eqs. (6), (10), and (11) with Eq. (5) to obtain the fully scaled Poisson equation:

$$\begin{aligned} \epsilon^2 \chi'' &= - \left( \sum_i n_i - n_e \right) / n_0, \\ \epsilon &= \lambda_0 / \lambda. \end{aligned} \quad (12)$$

The parameter  $\epsilon$  is required to be small for the applicability of the present model to a plasma. Equation (12) is the starting point for all of the following discussion.

### 3. The regions of the plasma

From an analysis point of view, the distinct regions of the plasma are defined by the approximations to the general EOM that afford certain approximate solutions, which describe the plasma within those regions. Here, we will consider the plasma to be decomposed into three regions: (1) a bulk quasineutral ambipolar-diffusion region, (2) a presheath quasineutral region with nondiffusive ion motion, and (3) the non-neutral, noncollisional sheath transition region. A fourth region, the Child–Langmuir region of low-electron density, could be added for QSS sheaths. This discussion is necessary to develop boundary conditions for the sheath model at the bulk plasma interface, and also to develop relations for multiple ions.

*a. Bulk ambipolar diffusion region.* This analysis begins with the full time-dependent set of EOM. First, we set  $\epsilon$  to zero in Eq. (12). This is an analytical way of stating that we are investigating the plasma in those regions where the spatial variations are very small on the scale of the Debye length. The resulting (asymptotic) solution requires  $n_e = \sum n_i$ , i.e., plasma neutrality. The ion momentum Eq. (2) is crucial for the next step in this analysis. If the ion velocities are small (but not too small, i.e., thermalized) compared to the Bohm velocities, it may be shown<sup>21</sup> that only the terms in Eq. (2) giving the balance between field acceleration and collisional drag are important, i.e.,

$$\frac{e}{m_i} E = v_i u_i, \quad (13)$$

$$E_i = \frac{1}{2} m_i u_i^2 \approx \frac{1}{2} \lambda e E.$$

The ion energy in Eq. (13) was evaluated using Eq. (8), which shows that all ions have about the same energy as they move in the ambipolar field, if the cross sections are only a function of ion mean energy. Equation (13) is another way of expressing Eq. (9). The usual ambipolar diffusion coefficient  $D_i$  can be introduced after rearranging the flux expression obtainable from Eq. (13)

$$n_i u_i = -D_i \frac{n_i}{n_e} n_e', \quad (14)$$

$$D_i \equiv \frac{kT_e}{m_i v_i},$$

where, again, we identified the collision frequency by assuming that it is dominated by the drift velocity. Of course, we have used the form of the ambipolar diffusion coefficient in which the electron temperature is much higher than the ion temperature.<sup>22</sup> The two primary conditions required for accuracy of this approximation are that the plasma be quasineutral and that the ion velocity be less than the Bohm velocity. The important point for the present work is that different positive ions appear to possess the same kinetic energy as they move towards the surrounding walls and encounter the presheath and sheath regions. This analysis also suggests that the ambipolar diffusion model may be adequate for the bulk description once we know how to impose boundary conditions on the plasma at or near the walls.

*b. The presheath region.* This is basically an “ion mean-free-path’s worth” of the plasma near the wall, but not including the sheath itself. Again, start the analysis with Eq. (12) by setting the dimensionless parameter  $\epsilon$  to zero to obtain quasineutrality. The difference here is that the ion velocities are on the order of the Bohm velocities, i.e., not assumed “small” as in the preceding section. To proceed, we must make more approximations to the basic EOM. We invoke the quasisteady state in addition to quasineutrality. From the QSS continuity equation, neglecting the source term in this low-collisional region as a matter of convenience, we have

$$(n_i u_i)' = 0. \quad (15)$$

This is just conservation of flux for each ion. We substitute the Boltzmann Eq. (4) into Eq. (2), invoke QSS, and have

$$u_i u_i' = -\frac{kT_e}{m_i} \frac{n_e'}{n_e} v_i u_i, \quad (16)$$

whereupon we immediately introduce the collision frequency and common ion mean-free path from Eqs. (8) and (10) to have

$$u_i u_i' = -\frac{kT_e}{m_i} \frac{n_e'}{n_e} u_i^2 / \lambda. \quad (17)$$

There is an ion-species dependence in this equation in the mass term, which is removable by scaling of the velocities. We scale the ion fluid velocities with the individual ion Bohm velocities,<sup>22</sup> and remove *all* ion-species dependence from Eq. (17), namely,

$$u_i = u u_{Bi}, \quad (18)$$

$$u_{Bi} = \sqrt{kT_e / m_i},$$

and obtain

$$u u' + n_e' / n_e = -u^2 / \lambda. \quad (19)$$

Of course, the independence of species depends also on the boundary conditions to be applied. We have argued earlier in the preceding section that all ions have about the same energy in the ambipolar region, which determines the input to the presheath region. Obtaining a QSS ion acceleration equation independent of species identity is important for us to be able to specify the boundary conditions at the sheath region itself.

The log derivative of the electron density in Eq. (19) is related to the ions *via* continuity in Eq. (15) and the scaled velocities in Eq. (18):

$$(n_i u_i)' = 0,$$

$$n_i' / n_i = -u_i' / u_i = -u' / u,$$

$$\frac{n_e'}{n_e} = \frac{\sum n_i'}{\sum n_i} = -\frac{u'}{u} \frac{\sum n_i}{\sum n_i} = -\frac{u'}{u}. \quad (20)$$

Thus, the simplified QSS EOM in the presheath region may be written, collecting from Eqs. (4), (15), (19), and (20), using the scaled velocities in Eq. (18),

$$\begin{aligned}
(n_i u)' &= 0, \\
u'(u - 1/u) + u^2/\lambda &= 0, \\
u'/u &= -\chi', \\
n_e &= \sum n_i.
\end{aligned} \tag{21}$$

Without loss of generality, we can impose boundary conditions of  $u = 1$  (Bohm velocity) at some position  $x = x_1$ . The analytic solutions  $u(x)$  and  $\chi'(x)$  to Eq. (21) can be expressed in terms of that one integration constant, which is the location of the sheath transition point,

$$\begin{aligned}
x &= x_1 - \lambda \ln(u) - \lambda \frac{1}{2}(1/u^2 - 1), \\
-\lambda \chi' &= u^2/(1 - u^2).
\end{aligned} \tag{22}$$

Recall that  $-\chi'$  is the scaled electric field as in Eq. (6). Equation (22) is an implicit solution for  $u(x)$ . One finds from Eq. (22) the well-known *singularity* in the field predicted by the quasineutral fluid EOM as the ion velocity approaches the Bohm velocity.<sup>23–25</sup> Of importance here is the fact that all ions approach the singularity at a common point  $x_1$ , at least within the limitations of our simplified analysis of the ion scattering behavior.

The ambipolar approximation derived in the preceding section should be contained within the quasineutral approximation appropriate for the presheath region, except for the time dependence. If we assume that  $u$  is less than unity, the field expression in Eq. (22) approximates to  $-\chi' \approx u^2/\lambda$ , which is the same as may be derived from the first member of Eq. (13), once having undone the velocity and potential scaling.

*c. The sheath transition region.* In the previous sections, we obtained approximate asymptotic solutions to the plasma fluid EOM by using the ratio of the Debye length to the ion collision length ( $\epsilon$ ) as a smallness parameter. Setting  $\epsilon \rightarrow 0$  gave quasineutrality. The solution broke down at the point in space where the ion fluid velocity reached the Bohm velocity. Thus, there is a nonuniformity involved in the approximation, and this should be corrected by a different asymptotic analysis. The limit of  $\epsilon \rightarrow 0$  must be supplemented by a coordinate scaling that leads to a *uniform* solution in the vicinity of the sheath transition point without requiring quasineutrality. A distinct description of this problem is the “two-scale” asymptotic analysis as presented in the review of Riemann.<sup>27</sup> In retrospect, we regret not making use of Riemann’s work in this preliminary analysis surrounding the new unified model developed in Sec. III B. The multifluid work of Benilov<sup>28</sup> and of Valentini and Herrmann<sup>29</sup> is also relevant to the preliminary analysis and regional matching.

Begin with Eqs. (1), (2), and (4). The space coordinate is now “stretched,”<sup>30</sup> about the singular point by substituting  $x = x_1 + \epsilon z$  into the equations. The space derivatives become  $\partial/\partial x \rightarrow (1/\epsilon)\partial/\partial z$  and dominate the equations as  $\epsilon \rightarrow 0$ . The time derivatives are also assumed large in the scaled EOM. Equation (12) already contains  $\epsilon$  and the coordinate scaling simply cancels out the dependence. Only the zero-order terms in a Taylor expansion in  $\epsilon$  of the dependent variables

are retained. The net result is an approximate asymptotic set of EOM corresponding to Eqs. (1)–(5). If we undo all the scaling in the limiting equations [except for the potential as in Eq. (6)], the result is the collisionless EOM,

$$\begin{aligned}
\dot{n}_i + (n_i u_i)' &= 0, \\
\dot{u}_i + u_i u_i' + \chi' u_{Bi}^2 &= 0, \\
n_e'/n_e &= \chi', \\
\chi'' &= -\frac{e^2}{\epsilon_0 k T_e} \left( \sum_i n_i - n_e \right).
\end{aligned} \tag{23}$$

One sees that stretching is a formal way of approximating the EOM appropriate for the small sheath dimension. These equations could be further integrated in the QSS approximation<sup>19</sup> by substituting the  $n_e$  and  $n_i$  dependence on  $\phi$  into the Poisson equation. This would generate the so-called first integral of the second-order Poisson equation, which relates the electric field and potential. It enables the development of the adiabatic sheath model of MEO.<sup>19</sup>

It is worth understanding the limitation of Eq. (23) due to the stretching transformation,<sup>30</sup> which was used to derive it. The solution to Eq. (23) is only valid within a small region about the point  $x_1$ . Nevertheless, this is a very important region of the plasma, as the above solution no longer requires neutrality and the equations can be interpreted as the collisionless free fall of the ions from the bulk to the material wall. The discussion in the preceding two sections showed how to connect the solutions of Eq. (23) to the presheath solutions. That analysis showed that all singly charged positive ions tend to approach the common singular space point with their Bohm velocities, at least in the QSS limit. The stretching transformation, which is the same as a coordinate scaling with the *Debye length*, has been used to generate an approximation, which is not singular at that point. A more detailed analytical and numerical analysis for a single ion species has been given before.<sup>21</sup>

## B. Time-dependent ion motion within the sheath

We begin with Eq. (23) and switch to  $x_1$  as the position of the reference point. The Boltzmann relation for the electron distribution in Eq. (23) is rewritten in integrated form,

$$\begin{aligned}
\dot{n}_i + (n_i u_i)' &= 0, \\
\dot{u}_i + u_i u_i' + \chi' u_{Bi}^2 &= 0, \\
\chi'' &= -\frac{e^2}{\epsilon_0 k T_e} \left( \sum_i n_i - n_1 \exp(\chi) \right).
\end{aligned} \tag{24}$$

The boundary conditions appropriate for the solution are

$$\begin{aligned}
n_e(x_1) &= \sum_i n_i(x_1) \equiv n_1, \\
\chi(x_1) &= 0, \\
u_i(x_1) &= u_{Bi},
\end{aligned} \tag{25}$$

all at the common Bohm point as argued in the previous section. A more rigorous analysis also supports this assumption.<sup>31</sup>

We must now approximate the solution to Eq. (24) in order to obtain a practical result similar to the MEO model.<sup>19</sup> Basically, the time-dependent motion of each ion is approximated by the adiabatic motion within a new potential field  $\bar{\phi}_i$ , or its scaled equivalent,  $\bar{\chi}_i = e(\bar{\phi}_i - \phi_1)/kT_e$ , which must be determined. The  $\bar{\chi}_i$  are all zero at the point  $x_1$  and  $\phi_1$  can be time dependent.  $\phi_1$  is usually taken as the plasma potential. The ion density and velocity are assumed to satisfy the conservative flux and energy relations with a parametric time dependence contained in  $\bar{\phi}_i$ ,

$$n_i u_i \approx n_i(x_1) u_i(x_1) \equiv n_{1i} u_{Bi}, \quad (26)$$

$$\frac{1}{2} m_i u_i^2 + e \bar{\phi}_i \approx \frac{1}{2} m_i u_{Bi}^2 + e \phi_1.$$

The last relation in Eq. (26) reduces to

$$\frac{1}{2} u_i^2 / u_{Bi}^2 + \bar{\chi}_i = \frac{1}{2}, \quad (27)$$

$$u_i = u_{Bi} (1 - 2\bar{\chi}_i)^{1/2},$$

Time is an implicit variable in all of Eqs. (26) and (27), as elsewhere.

If we combine Eqs. (24), (26), and (27), we derive the following approximation for the sheath region:

$$n_i u_i \approx n_{1i} u_{Bi}, \quad \dot{\bar{\chi}}_i \approx -u_i (\bar{\chi}_i - \chi'), \quad (28)$$

$$\chi'' \approx -\frac{e^2}{\epsilon_0 k T_e} \left( \sum_i \frac{n_{1i}}{\sqrt{1-2\bar{\chi}_i}} - n_1 \exp(\chi) \right).$$

The Poisson equation in Eq. (28) cannot be integrated exactly to form the first integral. A convenient means of approximating the Poisson equation is to assume that the ion potentials are related to the actual potential by a function of time, i.e.,

$$\bar{\chi}_i \approx \alpha_i(t) \chi. \quad (29)$$

This *ansatz* given in Eq. (29) has motivations based on the approximations for the first integral of the Poisson equation.<sup>20</sup> Substitution of Eq. (29) into the second and third members of Eq. (28) allows the first integral to be performed on the Poisson equation, giving rise to one new constant of integration,  $\chi'_1$ . After the integration is performed,  $\alpha_i(t)$  is replaced by  $\bar{\chi}_i/\chi$  to give

$$\begin{aligned} \dot{\bar{\chi}}_i &= -u_i \frac{\chi'}{\chi} (\bar{\chi}_i - \chi), \\ \frac{1}{2} (\chi')^2 &\approx \frac{1}{2} (\chi'_1)^2 + \frac{e^2 n_1}{\epsilon_0 k T_e} \left( \sum_i \frac{n_{1i}}{n_1} \frac{\chi}{\bar{\chi}_i} (\bar{u}_i - 1) + e^\chi - 1 \right), \\ \bar{u}_i &\equiv (1 - 2\bar{\chi}_i)^{1/2}. \end{aligned} \quad (30)$$

This procedure for obtaining the first integral becomes exact in the case of the adiabatic limit of MEO,<sup>19</sup> where  $\alpha_i(t)$  remains unity. The first equation in Eq. (30) has the form of

a damping or relaxation equation if the prefactor can be replaced by a constant. It may be argued that the prefactor is of the order of the plasma ion frequency

$$O\left(u_i \frac{\chi'}{\chi}\right) = u_{Bi} \frac{1}{\lambda_1} = \omega_{pi}, \quad (31)$$

where  $\lambda_1$  is the Debye length at  $x_1$ . The equations for determining the ion potentials reduce to the damping equation for each ion

$$\dot{\bar{\chi}}_i \approx -\omega_{pi} (\bar{\chi}_i - \chi). \quad (32)$$

Equation (32), combined with the voltage-field first integral in Eq. (30), are the equations to be used to determine the effective ion response in a varying potential field. We note that the use of the ion plasma frequency as a universal damping constant for the ion response is a newer and simpler aspect of the unified sheath model that appears consistent with the approximations used in the derivation. Possibly, this could need improvement for strongly biased plasmas.

Recall that the actual potential in the sheath, as well as the ion potentials, are obtained by undoing the scaling and zero shift

$$\begin{aligned} \chi &= e(\phi - \phi_1)/kT_e, \\ \bar{\chi}_i &= e(\bar{\phi}_i - \phi_1)/kT_e. \end{aligned} \quad (33)$$

Thus, the gradient of  $\chi$  is related to the field by  $\chi' = -eE/kT_e$ . It is now appropriate to reintroduce the electric field into Eq. (30) and to write down the two partial derivatives needed in the circuit analysis:

$$\begin{aligned} \frac{1}{2} E^2 &= \frac{1}{2} E_1^2 + \frac{n_1 k T_e}{\epsilon_0} \left( \sum_i \frac{n_{1i}}{n_1} \frac{\chi}{\bar{\chi}_i} (\bar{u}_i - 1) + e^\chi - 1 \right), \\ E \frac{\partial E}{\partial \chi} &= \frac{n_1 k T_e}{\epsilon_0} \left( \sum_i \frac{n_{1i}}{n_1} \frac{1}{\bar{\chi}_i} (\bar{u}_i - 1) + e^\chi \right), \\ E \frac{\partial E}{\partial \bar{\chi}_i} &= \frac{n_{1i} k T_e}{\epsilon_0} \frac{\chi}{\bar{\chi}_i^2} (1 - \bar{u}_i - \bar{\chi}_i / \bar{u}_i). \end{aligned} \quad (34)$$

The scaled velocity has been defined in Eq. (30).

The constant of integration  $E_1$  is yet to be determined. A difficulty that is found immediately is that the right-hand side (RHS) of the first member of Eq. (34) can be negative at certain phases within the period of the rf bias, giving an imaginary value for the electric field. The boundary conditions used here are that the electric field at the Bohm point is greater than or equal to zero and this value should be large enough to force the RHS of the top equation in Eq. (34) to be non-negative at whatever spatial position we evaluate  $E(\chi, \{\bar{\chi}_i\})$ . Only for large applied bias fields will  $E_1$  need to be nonzero. Equation (34) reduces to the QSS MEO theory in the limit of slow time variation. In this limit, the constant  $E_1$  can be identically zero, although better estimates are known.<sup>32</sup> Two time-dependent numerical procedures come to mind to find  $E_1$ : (1) instantaneously set  $E_1(t)$  such that the RHS of Eq. (34) is non-negative as the time-dependent EOM are being solved numerically, and (2), let  $E_1(t)$  “ride up” numerically to a constant value such that the RHS of Eq. (34) remains positive. In the first procedure, the time deriva-

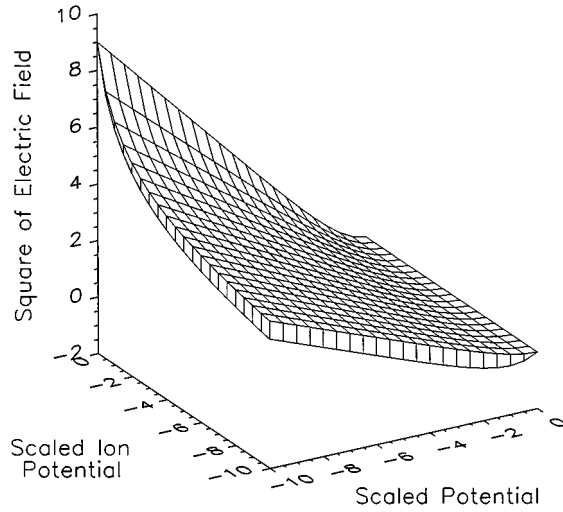


FIG. 1. The approximate first integral of the Poisson equation for the case of a single ion species. The top section of the surface is the non-negative approximation as given in Eq. (35). The surrounding vertical skirt shows the difference from the result in Eq. (34) with  $E_1$  set to zero. The difference is not great except in the region of small  $\chi$  (scaled potential) and large  $\bar{\chi}_i$  (scaled ion potential), which occurs during only a small part of the rf cycle.

tive of  $E$  is zero during the interval that  $E_1(t)$  is forced to be nonzero. In the second procedure, the time derivative of  $E_1(t)$  can be ignored as it becomes constant after a few rf cycles. A third purely analytic procedure for avoiding the imaginary field value is to modify the expression for  $E^2$  in a reasonable manner. Analysis of the problematic region suggests the non-negative form

$$\begin{aligned} \frac{1}{2} E^2 &= \frac{n_1 k T_e}{\epsilon_0} \left( \sum_i \frac{n_{1i}}{n_1} \frac{(\bar{u}_i - 1)}{\bar{\chi}_i} \right) (1 + \chi - e^\chi), \\ E \frac{\partial E}{\partial \chi} &= \frac{n_1 k T_e}{\epsilon_0} \left( \sum_i \frac{n_{1i}}{n_1} \frac{(\bar{u}_i - 1)}{\bar{\chi}_i} \right) (1 - e^\chi), \\ E \frac{\partial E}{\partial \bar{\chi}_i} &= \frac{n_{1i} k T_e}{\epsilon_0} \frac{(1 - \bar{u}_i - \bar{\chi}_i / \bar{u}_i)}{\bar{\chi}_i^2} (1 + \chi - e^\chi). \end{aligned} \quad (35)$$

The difference of this expression for the first integral of the Poisson equation from the result in Eq. (34) is shown in Fig. 1. The numerical solutions to be presented later in this paper used the second of the suggested numerical procedures. In general though, the analytical modification presented in Eq. (35) is neater and does not give significantly different results as has been demonstrated in unpublished computations.

### C. The sheath as a circuit element

The total current per area  $j_{\text{tot}}$  through the sheath is expressed as the sum of the electron, ion, and displacement currents:

$$j_{\text{tot}} = j_e + j_{\text{ion}} + j_d, \quad (36)$$

which is constant across the sheath if the full time-dependent continuity and Poisson's equations are being solved consistently. Here, we are using approximations to the dynamics, so the expression is only approximately independent of  $x$ . All three terms on the RHS of Eq. (36) must be evaluated

from the plasma sheath variables. The electron current per area to the wall,  $j_e$ , is approximated from kinetic theory as

$$\begin{aligned} j_e &= -\frac{1}{4} e v_e n_e(x_w), \\ v_e &= (8kT_e / \pi m_e)^{1/2}, \end{aligned} \quad (37)$$

where  $x = x_w$  is the wall position and  $v_e$  is the thermal velocity of the electrons. The electron density at the wall is obtained from the Boltzmann Eq. (4) using the Bohm point as the reference. The ion current per area to the wall is obtained by flux conservation from the specified values at the Bohm point:

$$\begin{aligned} j_{\text{ion}} &= \sum_i j_i, \\ j_i &= e n_i(x_w) u_i(x_w) = e n_{1i} u_{Bi}. \end{aligned} \quad (38)$$

It should be noted that a constant or slowly varying ion current is a basic limitation of our sheath model. The electron displacement current  $j_d$  should be evaluated at the wall position to be consistent with both the point of determination of  $j_e$  and the later connection to be developed to the complete rf circuit. The displacement current is expressed as the partial time derivative of the field at the wall. The time derivative of  $E$  now necessitates the evaluation of all partial derivatives in order to find  $\dot{E}$  by the chain rule and, thus,  $j_d(t)$ ,

$$j_d(t) = \epsilon_0 \dot{E} = \epsilon_0 \left( \frac{\partial E}{\partial \chi} \dot{\chi} + \sum_i \frac{\partial E}{\partial \bar{\chi}_i} \dot{\bar{\chi}_i} \right). \quad (39)$$

These partial derivatives are found from Eq. (34) or (35), which give  $E(\chi, \{\bar{\chi}_i\})$  and the partials explicitly.

Consider an element of sheath area  $A_k$ , which can be of any size, perhaps the whole electrode itself. The current through the element is just

$$I_k = A_k j_{\text{tot}}, \quad (40)$$

where  $j_{\text{tot}}$  is to be evaluated from properties appropriate to the  $k$ 'th electrode element. Functionally, we know that the total current density through the area element is the sum of the components as in Eq. (36), and we also know that the electron particle current is a function of the potential difference between the wall and the plasma reference point as given in Eqs. (4) and (37),

$$\begin{aligned} j_{\text{tot}} &= j_{\text{tot}}(j_e, j_{\text{ion}}, j_d), \\ j_e &= j_e(\chi), \\ j_{\text{ion}} &= \text{given}. \end{aligned} \quad (41)$$

The ion current density is a given (fixed) quantity within the assumptions of the sheath model solution. From Eqs. (39) and (32), we have the functional dependence of the electron displacement current,

$$\begin{aligned} j_d &= j_d(\chi, \dot{\chi}, \{\bar{\chi}_i\}, \{\dot{\bar{\chi}_i}\}), \\ \dot{\bar{\chi}_i} &= \dot{\bar{\chi}_i}(\chi, \bar{\chi}_i). \end{aligned} \quad (42)$$

Combining Eqs. (41) and (42), we have the relations

$$\begin{aligned} j_{\text{tot}} &= j_{\text{tot}}(\chi, \dot{\chi}, \{\bar{\chi}_i\}), \\ \dot{\bar{\chi}_i} &= \dot{\bar{\chi}_i}(\chi, \bar{\chi}_i), \end{aligned} \quad (43)$$



which are all that is needed to form the circuit equations with the coefficient of  $\dot{\chi}$  identified as an effective capacitance and the rest as a nonlinear resistance or voltage source.

We should mention that the rf-biased, inductively driven case that we are addressing here is simpler than the system investigated by Nitschke and Graves<sup>33</sup> because we are treating the rf bias of the sheath as a perturbation on the bulk plasma. The power input in Ref. 33 has a large or dominant amount of capacitive coupling, and in such a case, the bulk and sheath EOM's are strongly coupled, and we could not have specified boundary conditions as easily as done here. Nitschke and Graves used Godyak and Sternberg's model,<sup>24</sup> which is physically much the same as Lieberman's<sup>18</sup> high-frequency model of ion response. Nitschke and Graves' conclusion was that their sheath model was useful even in the regions where one might expect the model to be invalid.

#### IV. RF-CIRCUIT MODELS

This section describes the two different rf-circuit models that were involved in this work. The principal rf-circuit model was used to develop a set of differential equations that were solved simultaneously with the equations of Sec. III for the sheath behavior. That principal model is described in Sec. IV A. Another, separate rf-circuit model was used solely for data reduction. The data-reduction model, described in Sec. IV B, was used to convert measured values of the rf potential and current to values at the lower electrode. The data-reduction model treated rf circuitry that was a subset of the circuit treated by the principal model. The data-reduction model was used with the data-acquisition computer as part of the data-acquisition process.

##### A. Principal model

It is necessary to include a detailed rf-circuit model as part of the plasma-sheath calculations because plasma sheaths are electrically nonlinear. The nonlinearity causes the generation of electrical signals at harmonics of the fundamental excitation frequency, and at subharmonics under some conditions.<sup>34,35</sup> The rf circuitry, which provides single-frequency excitation at the fundamental frequency, also presents an impedance to the plasma at each harmonic frequency. The plasma is the source of the harmonics and the rf circuit is a load for the harmonics. Consequently, the ratio of the rf potential to the rf current at each harmonic frequency is equal to the impedance of the rf circuit at that frequency.<sup>36</sup> For example, potential (or current) at a particular harmonic frequency can be suppressed if the rf circuit has low (or high) impedance at that harmonic frequency. In addition, if the rf circuit impedance at a harmonic frequency is purely reactive, then no net power can leave the plasma at that harmonic frequency. If these effects are not combined properly with the plasma model, then the calculations of the harmonic levels will be incorrect.

The foregoing implies that an accurate model of the *entire* rf system must be connected to the plasma-sheath model. However, previous work<sup>37</sup> suggests that it may be sufficient to model accurately only those rf components that are exposed to significant harmonic signals and, thereby, significantly affect the circuit impedance as seen by the plasma at

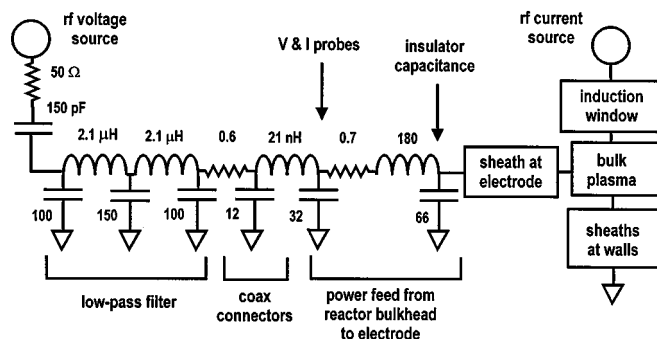


FIG. 2. Schematic of the principal rf-circuit model discussed in Sec. IV A coupled to the plasma-sheath model. The rf-circuit model accurately represented only those components that were accessible to the plasma-generated harmonics. Both rf sources are sinusoidal 13.56 MHz sources. The rf current source represented the capacitive coupling from the induction coil to the bulk plasma. Component values are given in ohms, picofarads, and nanohenries, except for the filter inductances, which are in microhenries. The component values were based on vector-impedance-meter measurements. The model component values near the electrode differed from those used in data reduction because this circuit model represented additional hardware that was not involved in data reduction.

the harmonic frequencies. For our experiment, a low-pass filter was connected in series with the power feed to the lower electrode, and the rf-circuit model treated accurately only the filter and the electrical components between the filter and the lower electrode. This simplified the circuit model greatly. Note that this approach does not compute accurately the impedance at the fundamental frequency that the lower electrode presents to the current which is capacitively coupled into the plasma from the induction coil. In cases where the capacitive current is dominant, this treatment could give inaccurate results.

The circuit model for the calculations is shown in Fig. 2. The component values were determined by the methods described below in Sec. V C 2. The circuit model explicitly contained circuit elements representing (1) the low-pass filter, (2) the coaxial connectors that led from the filter box to the reactor bulkhead, (3) reactances of the rf potential and current sensors, and (4) the power feed to the lower electrode. Electrical power was applied in the model by a voltage source connected to the filter through a series resistor and a capacitor. These latter components were not exposed to harmonic signals, and thus, did not represent directly any actual physical components in the experimental apparatus.<sup>38</sup> They merely provided a convenient and stable way to supply power *via* the mathematical model. Note that the series capacitor allowed the development of dc bias at the lower electrode. The rf circuit in Fig. 2 includes 11 separate inductors and capacitors. In the calculations, we combined the 12 pF capacitor with the adjacent 100 pF capacitor and we moved the 0.6  $\Omega$  resistor in series with the adjacent 2.1  $\mu$ H inductor. This eliminated one short time constant and did not affect the results. Consequently, the circuit was described by ten coupled ordinary differential equations (ODEs).

Figure 3 is an expansion of the plasma region shown in Fig. 2 that defines current-flow nomenclature. The bulk plasma was treated as a current node connected to three current paths:  $I_{\text{bias}}(t)$  flowed from the rf-biased electrode into

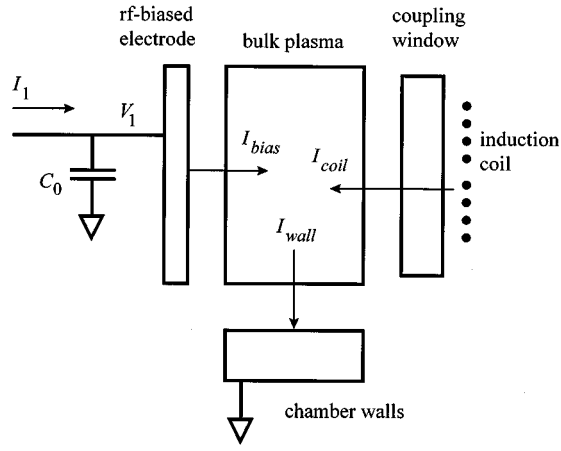


FIG. 3. Schematic of the plasma region defining current flows through the plasma sheaths into and out of the bulk plasma as used in Eq. (44).

the bulk plasma;  $I_{\text{coil}}(t)$ , a displacement current, flowed from the induction coil, through the coupling window, into the bulk plasma; and  $I_{\text{wall}}(t)$  flowed from the bulk plasma to the chamber walls. Current continuity required

$$I_{\text{coil}} + I_{\text{bias}} = I_{\text{wall}}. \quad (44)$$

The current from the rf-circuit components to the biased electrode was denoted  $I_1(t)$  and the electrode potential  $V_1(t)$ . The capacitance shunting the electrode to ground was  $C_0$  and

$$I_1 = I_{\text{bias}} + C_0 \dot{V}_1. \quad (45)$$

The series impedance of the thick coupling window was assumed to be much greater than the impedance of the thin plasma sheath at the coupling window. Consequently, the current  $I_{\text{coil}}$  was simply a displacement current given by the time derivative of the difference in local coil potential  $V_{\text{coil}}(r, t)$  and local plasma potential  $V_p(r, t)$ ,

$$I_{\text{coil}} = \sum_k dA_k [C_w (\dot{V}_{\text{coil}} - \dot{V}_p)]|_k, \quad (46)$$

where the summation over  $k$  denotes summation over spatial zones, of area  $dA_k$ , that were used in the computation to describe the window and coil. The currents through the plasma sheaths at the biased electrode and the walls are described by Eqs. (36), (38), and (39), with  $\phi_1 = V_p$ . For thoroughness, we rewrite those equations as they apply to the geometry of our experiment, and for a single ion species, as

$$I_{\text{bias}} = \sum_k dA_k \left[ j_e + j_i + \epsilon_0 (\dot{V}_p - \dot{V}_1) \frac{\partial E}{\partial V} + \epsilon_0 \omega_{pi} (\bar{V} - V_1) \frac{\partial E}{\partial \bar{V}} \right]_k, \quad (47)$$

and

$$I_{\text{wall}} = \sum_k dA_k \left[ -j_e - j_i - \epsilon_0 \dot{V}_p \frac{\partial E}{\partial V} - \epsilon_0 \omega_{pi} \bar{V} \frac{\partial E}{\partial \bar{V}} \right]_k. \quad (48)$$

Equations (47) and (48) are similar to each other. The summations are over the pertinent spatial zones for the biased electrode and the chamber walls. The sign differences in these two equations arise because of the choice of current directions in Fig. 3, and Eq. (48) has “missing” potential terms because the wall potential was defined as zero.

In Eq. (47),  $\dot{V}_1$  does not depend on  $k$  (the electrode was an equipotential surface), and in Eqs. (47) and (48),  $\dot{V}_p$  does not depend on  $k$  (a consequence of the bulk plasma model in Sec. II). Thus, Eqs. (44)–(48) were combined to yield two simultaneous equations in  $\dot{V}_p$  and  $\dot{V}_1$ , which were further separated to provide one ODE for  $\dot{V}_p$  and one for  $\dot{V}_1$ . The electric field derivatives in Eqs. (47) and (48) were given in Eq. (34), which we rewrite explicitly for thoroughness as

$$\frac{\partial E}{\partial V} = \frac{n_1 e}{\epsilon_0 E} \left[ \frac{\sqrt{1 - 2e(\bar{V} - V_p)/kT_e} - 1}{e(\bar{V} - V_p)/kT_e} + \exp[e(V - V_p)/kT_e] \right], \quad (49)$$

$$\frac{\partial E}{\partial \bar{V}} = \frac{n_1 kT_e}{\epsilon_0 E} \frac{(V - V_p)}{(\bar{V} - V_p)^2} \left[ 1 - \sqrt{1 - 2e(\bar{V} - V_p)/kT_e} - \frac{e(\bar{V} - V_p)/kT_e}{\sqrt{1 - 2e(\bar{V} - V_p)/kT_e}} \right], \quad (50)$$

and

$$E^2 = E_1^2 + \frac{2n_1 kT_e}{\epsilon_0} \left[ \frac{(V - V_p)}{(\bar{V} - V_p)} (\sqrt{1 - 2e(\bar{V} - V_p)/kT_e} - 1) + \exp[e(V - V_p)/kT_e] - 1 \right]. \quad (51)$$

The equation describing  $\bar{V}$ , based on Eq. (32), is

$$\dot{\bar{V}}_k = \dot{V}_p - \omega_{pi} (\bar{V}_k - V_k), \quad (52)$$

with one equation of this form appearing for each zone of the biased electrode and of the chamber wall.

For the calculations reported below, the spatial variations in the plasma parameters were represented in the sheath model by using five radial zones at the biased lower electrode and three zones at the grounded walls of the reactor. The total number of simultaneous first-order ODEs employed for the calculations, thus totaled 19: ten equations for the circuit potentials and currents (including the equation for  $V_1$ ), one equation for  $V_p$ , and one equation for  $\bar{V}$  in each of the eight zones. The equations were integrated using a fourth-order Runge–Kutta method, with a typical solution for 100 rf cycles requiring approximately 1 min on a personal computer.<sup>39</sup>

## B. Data-reduction model

Measurement of *electrode* potential and current was made more complicated because the potential and current sensors actually measured potential and current at a point on the power feed leading to the electrode, not at the electrode

itself. The distance along the power feed from the sensors to the electrode was 40 cm. The 40 cm length of the power feed had an inductance of approximately 130 nH. The electrode had a shunt capacitance to ground through its Teflon insulator of approximately 80 pF. These two parasitic reactances caused the potential and current at the electrode to differ substantially from the measured values of potential and current. One approach to this problem would be to compare potentials and currents in the model and the experiment at the sensor location rather than at the electrode. The principal circuit model (Sec. IV A) intrinsically must have the capability to generate this output because it must include a detailed model of the rf circuitry connected to the lower electrode. However, it seemed more appealing to compare the parameters at the electrode because they were more intimately tied to the plasma sheath. This choice necessitated use of a technique to compute electrode potential and current from measured potential and current.

To compute electrode potential and current, we used an equivalent-circuit model for data reduction that had been developed previously to represent the power-feed hardware between the sensors and the lower electrode. The data reduction used an approach directly related to the one described in Ref. 40. In that approach, an equivalent-circuit model is developed that is based on the physical geometry of the hardware. The simplest model, suggested in the preceding paragraph, would have a series inductance  $L$  leading from the sensors to the electrode and a shunt capacitance  $C$  from the electrode to ground. With rf excitation at frequency  $\omega$  applied to an empty reactor (no plasma), the impedance  $Z$  (a complex phasor quantity) at the sensor location for this model is

$$Z = j\omega L + 1/j\omega C, \quad (53)$$

where  $j$  is the imaginary unit. Values of  $L$  and  $C$  may be determined by applying excitation at two different frequencies and by measuring the impedances indicated by the sensors. If the computed and measured impedances are set equal for both measurements, then two equations in two unknowns ( $L$  and  $C$ ) result, and  $L$  and  $C$  are determined uniquely. Note that the resulting value of  $C$  will include capacitance from the electrode surface to the inner volume of the reactor, which normally is filled by plasma. That extra capacitance should be subtracted from the final value used in the model. This two-frequency measurement also provides a method to correct for small phase-measurement errors. Within the context of the simple  $L$ – $C$  model, the two measured impedances must have phases of  $\pm 90^\circ$ . Deviations from the correct value can be corrected in the software to compensate for small phase errors in the sensors, cables, and oscilloscopes.

This two-frequency technique can be accomplished conveniently by exciting the lower electrode with a pulse train that is rich in harmonics rather than by using two separate sinusoidal excitations. Then, the two-frequency measurements and calculations can involve, for example, the fundamental and second harmonics, which can be treated separately in the frequency domain. The most convenient arrangement is with the repetition rate of the pulse train equal to the fundamental frequency of interest, i.e., 13.56

MHz for the present work. Then, all the frequency components of the pulse train occur at frequencies of interest for the plasma experiments.

The simple  $L$ – $C$  model is useful for illustrative purposes, but it has shortcomings, several of which have been addressed in detail by Sobolewski.<sup>41</sup> For example, the simple model ignores resistive losses and it may not accurately represent the actual distribution of parasitic reactances in the hardware. Neglect of resistive losses can lead to phase errors that lead to large power errors in plasma measurements if the potential-current phase angle is near  $\pm 90^\circ$ . The power loss in the resistance itself is usually a much smaller effect.

For the present studies, we tested several different physically based circuit models involving resistive losses and additional parasitic reactances. For each circuit model, we performed measurements at many harmonics and used a mathematical optimization technique<sup>42</sup> to adjust the model parameters for the best fit to the measured impedances at all the harmonics. In all cases, we used more harmonics than there were adjustable parameters in the circuit. This yielded an overdetermined set of equations for the circuit parameters. A valid circuit model should fit the data well at all frequencies. The final model that was used for the experiment consisted of a constant-impedance transmission line connecting the sensor location to the electrode, with shunt capacitances at both ends of the line. The electrical length of the transmission line was held fixed (0.116 rad at 13.56 MHz) and was equal to the length of the power-feed hardware represented by the line. The line's characteristic impedance and the shunt capacitances at the input and output of the line were variables that were chosen by the optimized fit to the harmonic measurements. Data from five harmonics were used to determine values of the three variables. This model gave only a slightly better fit to impedances at the five harmonics than did another three-variable models that used the simple  $L$ – $C$  model (above) along with an input shunt capacitor. In no model did we find the presence or absence of resistance (typically,  $< 1 \Omega$ ) to affect the results significantly for this experiment.

The reader should keep in mind that the circuit models discussed in this section were used as part of the experimental data-reduction process to obtain electrode potential and current. This data-reduction circuit model represented only a fraction of the rf circuitry in the experiment and was completely separate from the principal circuit model, discussed in Sec. IV A, that was used in conjunction with the plasma-sheath model.

## V. EXPERIMENTAL APPARATUS AND TECHNIQUES

In this section, we describe the experimental apparatus and data-acquisition techniques in detail. Note that there are many parts to the experimental procedures and measurements; all must be substantially correct in order to provide a valid test of the sheath model.

### A. Plasma reactor

Many aspects of the plasma reactor used in this work, a GEC reference cell, have been described in detail previously. The initial GEC cells were 13.56 MHz parallel-plate reactors

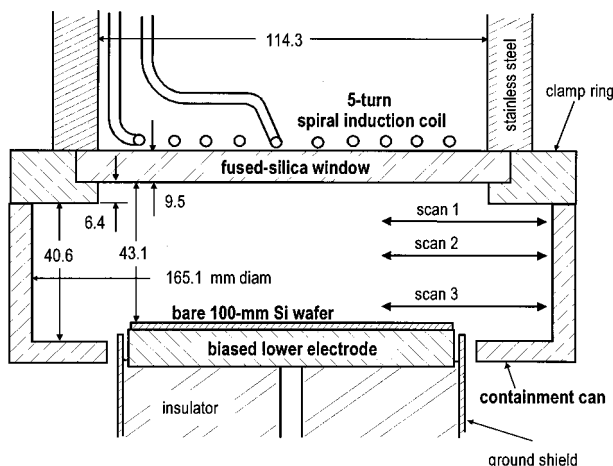


FIG. 4. Cross section of the modified GEC rf reference cell. Dimensions are shown in millimeters. The region around and above the induction coil was in the ambient laboratory atmosphere. The region inside and outside the containment can was inside the surrounding high-vacuum chamber. The radial scan paths were used to obtain the Langmuir-probe data in Fig. 9. Paths 1, 2, and 3 were 28.6, 19, and 5 mm above the wafer, respectively.

with 10 cm diam electrodes, as described in Ref. 40. The main purpose of the reactor originally was to enable inter-laboratory comparisons of measurements of discharge physics in a common, inexpensive device. It had excellent diagnostic access to the discharge volume but it did not have a provision for automated handling (clamping, cooling) of semiconductor wafers. At present, dozens of these reactors are in operation in laboratories throughout the world. Subsequently, an optional modification was developed<sup>43</sup> that replaced the upper electrode with an inductively coupled plasma source that generated higher density plasmas ( $10^{12}$  electrons/cm<sup>3</sup>) at lower pressures (1–20 mTorr). That new plasma source was based directly on earlier inductively coupled sources developed in industry.<sup>1–9</sup> The modification enabled discharge studies of plasmas in regimes more relevant to new generations of industrial reactors. The modified reactor still preserved excellent diagnostic access to the discharge volume via eight ports located in the equatorial plane of the discharge.

The studies reported here emphasized the flow of current from the lower, rf-biased electrode, through the plasma sheath, into the bulk plasma, and back to the reactor walls. The sheaths at the reactor walls were in series with the current path from the lower electrode, and thus, constituted an important part of the rf circuit.<sup>44</sup> In order to treat the sheaths at the reactor walls quantitatively, we needed to measure plasma properties near the walls using a Langmuir probe, as discussed in detail below. The problem with the GEC reference cell for these measurements was that the presence of the many ports in the reactor walls made the structure very much three-dimensional in nature. This would have made it exceedingly difficult to measure the plasma properties over the entire complex surface. Consequently, an additional piece of hardware, called a “containment can,” was added to the reactor. The modified reactor with the inductive source and the containment can is shown in Fig. 4. The containment can provided a geometrically simple, cylindrically symmetric,

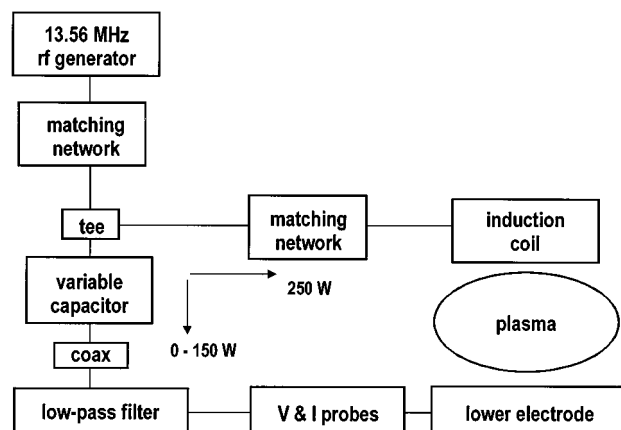


FIG. 5. Block diagram of the major rf components in the rf-excitation system. The variable capacitor in the rf-bias leg of the circuit was used to adjust the rf-bias level at the lower electrode. When the rf bias was changed, the rf generator was adjusted to maintain constant power to the induction coil.

grounded wall close to the discharge volume. Although the can defeated the reference cell’s otherwise-excellent diagnostic access, it provided a simple surface so that properties of the plasma sheath at the confinement wall could be measured easily with relatively few measurements.

Three axial slots, each 9 mm wide, were cut through the containment can to provide access for the Langmuir probe and to provide very limited visual access to the discharge volume. By bending the tip of the Langmuir probe, we were able to sample plasma near the inner walls of the containment can. Gas was injected into the reactor through the manifold at the bottom of the reaction chamber (originally designed as an exhaust manifold), and exhausted by a turbomolecular pump through a 6 in. side port. There was a circumferential gap, visible in Fig. 4, between the lower electrode and the containment can. Gas could enter and leave the discharge volume through this gap as well as through the axial slots in the can. This certainly provided adequate gas conduction for the experiments reported here, which did not involve chemical reactions that consumed the discharge gas. However, for studies involving rapid chemical reactions with a wafer, such as etching studies, the gas conduction could be inadequate.

A bare silicon wafer was placed on the lower electrode for the present experiments. The wafer prevented sputtering of metal from the lower electrode onto the fused-silica inductive-coupling window. In previous work, we had found that metal was sputtered rapidly when rf bias was applied, and the resulting conducting metallic coating on the window reduced the inductive excitation of the plasma. Sputtering of the silicon wafer did not give rise to such problems, probably because the sputtered material was not highly conducting.

## B. Rf excitation

A single 500 W rf generator operating at 13.56 MHz powered the induction source that sustained the bulk plasma and also provided rf bias to the lower electrode. A simple coaxial tee was used to connect the two branches of the system together, as shown in Fig. 5. The induction coil was

powered through an impedance-matching network containing two vacuum-variable capacitors, which was located immediately on top of the GEC cell. For all measurements, the network was tuned to maintain reflected power in that branch of the circuit below 1 W, according to an analog watt meter in that branch. Potential and current probes located between the induction coil and matching network showed very low levels ( $<1\%$ ) of harmonics. These low levels of harmonics were not particularly surprising because the coil and network constituted a high- $Q$  circuit tuned near 13.56 MHz. As a result,  $V_{\text{coil}}$  in Eq. (46) was taken to be a pure sinusoid at 13.56 MHz. This also means that the coil was treated as a grounded surface as far as plasma-generated harmonics were concerned.

The lower-electrode circuit was connected to the tee through a switch and a series variable coupling capacity (5–100 pF), which was varied to adjust the rf bias level. The switch was used to disconnect completely the rf generator from the lower-electrode circuit in order to obtain true, zero-rf-bias data. A low-pass filter was connected as close as was conveniently possible to the lower electrode in order to minimize the amount of circuitry that was exposed to plasma-generated harmonics. This reduced the complexity of the mathematical model of the rf circuitry involved with the harmonics. The branch of the rf circuit connected to the lower electrode did not include a matching network and, typically, had high reflected power (e.g., 50%). The length of the coaxial cable between the coupling capacitor and the low-pass filter was important for setting rf-bias levels. Only for a specific, empirically determined length of cable could the bias level be adjusted smoothly from below 1 W to over 150 W using the 5–100 pF range of the coupling capacitor.

The input impedance to the bias circuit appeared in parallel with the  $50\ \Omega$  impedance of the induction-coil branch of the circuit. To eliminate mismatches at the rf generator, a second matching network ( $\pi$  network) was used to connect the two branches of the rf circuit to the rf generator. As the variable coupling capacitor was adjusted to vary the rf bias, the rf generator output power was also adjusted to keep the induction-coil power constant. For a wide range of bias powers, the matching network connected to the induction coil required no retuning to maintain very low reflected power. This was one indication that the rf bias level did not significantly affect the parameters of the bulk plasma. This, of course, is one of the well-known advantages of this type of high-density plasma source.

## C. Rf electrical measurements

Electrical measurements formed the basis for much of our experimental data. Consequently, the hardware and analysis techniques described in this section are presented in some detail.

### 1. Rf potentials and currents

The comparisons between the model predictions and the experimental results consisted of comparisons of electrical signals. Those signals included computed and measured rf potential, rf current, rf power, and dc bias at the lower electrode under a variety of excitation conditions. Also compared

were the dc and rf components of the computed and measured plasma potential. The computations included capacitively coupled currents from the induction coil into the plasma. Consequently, the magnitude and phasing of the potential across the induction coil was required input into the model.

These many rf signals were all measured using two-channel 150 MHz digital oscilloscopes. The signals were acquired using a personal computer, Fourier transformed into the frequency domain, and manipulated as appropriate. Time synchronization of the signals was important. Signals from the induction coil, the plasma-potential probe, and the lower electrode were synchronized while exciting the induction coil without plasma (high-vacuum conditions). Under these conditions, the currents flowing inside the vacuum chamber were solely displacement currents proportional to the derivative of the coil potential. Consequently, it was straightforward to determine the correct relative phasing of all the signals. This knowledge enabled shifting the recorded signals by software to obtain proper phasing among the different oscilloscope channels. To minimize phase errors and sensitivity to signal shapes, the oscilloscopes were triggered for all experiments using a master pulse generator that was triggered by a signal coupled from the rf generator. The data-analysis computer code included provision for adjusting phases between different channels of a single oscilloscope as well as between different oscilloscopes. Once the proper phase shifts were determined from these vacuum measurements, the information was saved and used in all subsequent plasma measurements. Note that the relative phase of the coil current and the rf bias at the lower electrode were affected by changes in the rf-bias level made by changing the variable coupling capacitor. This changed the phasing of the capacitive coupling from the coil to the plasma. The measurements and calculations included this effect.

Potential and current were measured using custom-built capacitive and inductive sensors, respectively. They were physically compact and had good frequency response as a consequence of their geometry.<sup>40</sup> Their amplitude response was calibrated by comparison to commercial potential and current probes. The dc potential bias on the lower electrode was measured using a resistive voltage divider and a digital volt meter.

Based on previous work, we knew that the characteristic impedance ( $50\ \Omega$  nominal) of our coaxial cable (RG213/U) did not precisely match the input impedance ( $50\ \Omega$  nominal) of the digital oscilloscopes. Consequently, to minimize phase error, the rf data cables were adjusted to be one-half wavelength long ( $\lambda/2$ ) electrically at 13.56 MHz. In theory, this would minimize effects due to the cable–oscilloscope mismatches at 13.56 MHz and at the harmonics thereof. The cables were initially cut slightly too long. Then, they were connected to the oscilloscopes, the oscilloscopes' internal terminations were set to high impedance, and the input impedances of the coaxial cables were measured using a vector impedance meter. The cable lengths were then reduced until the input impedances peaked at 13.56 MHz. Figure 6 shows input–impedance data obtained with one of the adjusted  $\lambda/2$  cables. For this data, it is clear that phase errors of several

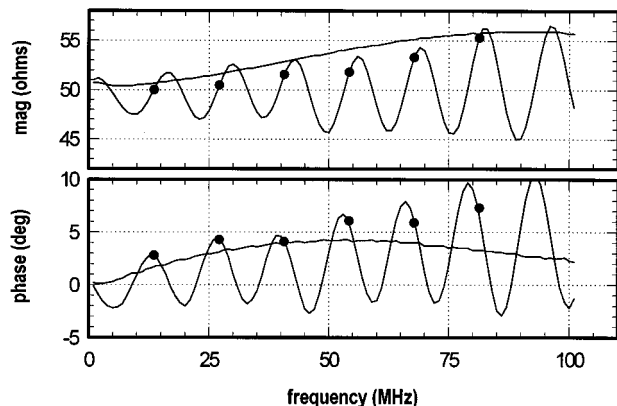


FIG. 6. Impedances of data-acquisition-system components. The smoother curves are the impedance measured by the vector-impedance meter at the input to a digital oscilloscope with the internal “50  $\Omega$ ” terminator activated. The oscillatory curves are the impedance at the input of a  $\lambda/2$  data cable (RG213/U) connected to the oscilloscope. The dots mark impedance values at multiples of 13.56 MHz. The  $\lambda/2$  cables reduced but did not eliminate phase errors that would be present with cables of other lengths.

degrees between harmonics still were present in the system because of the impedance mismatch of the cable and oscilloscope. The data analysis techniques discussed in Sec. IV B were able to reduce phase errors between, for example, potential and current at a particular harmonic frequency. However, those techniques could not eliminate phase errors between different harmonics.

## 2. Rf-circuit-impedance measurements

The principal rf-circuit model discussed in Sec. IV A and in Fig. 2 was developed and validated using a vector-impedance meter. Two main measurements led to the model. First, the low-pass filter was disconnected from the reactor, and the impedance at the output port of the filter was measured as a function of frequency from 1 to 110 MHz. The circuit model for the low-pass filter was then fitted to the data in the region above 15 MHz, where all the harmonics resided. An accurate model fit was obtained using the nominal design values for the filter components, with the addition of a 12 pF shunt capacitance at the output to the filter. That capacitance was probably associated with the coaxial connectors that were needed to interface to the impedance-meter probe. At frequencies below 15 MHz, the fit to the data depended on the load on the input port of the filter. Since the model did not attempt to include that part of the hardware, the data below 15 MHz were not used. Complete circuit characterization at lower frequencies would require dealing with the rf-generator impedance under power-on conditions. We are not certain how to perform that measurement.

Second, the impedance of the power feed to the lower electrode was measured at the point where the low-pass filter normally was connected. A model for the power feed involving a series inductance with two shunt capacitances (a pi network) was fitted to the data. This model was similar to one of the data-reduction models discussed at length previously (Sec. IV B) that was used in calculating potential and

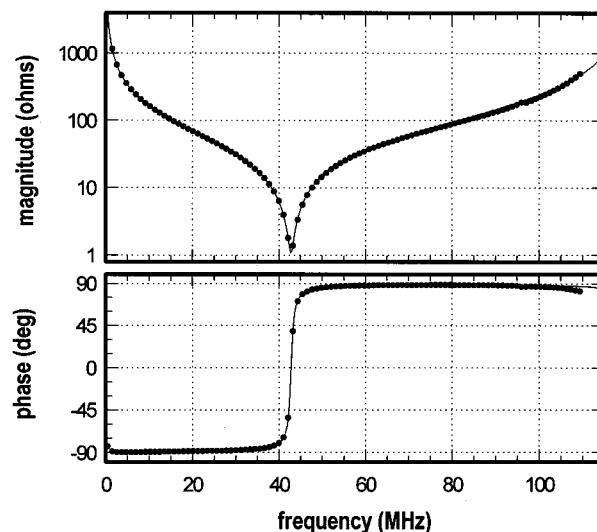


FIG. 7. Frequency-dependent impedance at the input to the power feed to the lower electrode. Dots are measured data points. The measurements were taken with the impedance meter under computer control and 1000 data points were taken. Only every 10th data point is shown here for clarity. The line is a fit to the data obtained for a pi network having an inductance of 171 nH with a series resistance of 1  $\Omega$ . This inductance included contributions from hardware between the voltage and current probes and the interface panel of the reactor. The shunt capacitances in the fit were 81 pF (insulator and electrode) and 12 pF (probes and panel connections).

current at the lower electrode. However, the models were not identical because one model included additional power-feed hardware. A comparison between the measured and calculated impedances of the power feed and lower electrode is shown in Fig. 7.

## D. Langmuir probe

A Langmuir probe was used to measure electron density, electron temperature, and the dc component of the plasma potential in the bulk plasma. These values were needed as input to the sheath model. The probe techniques were described previously in Ref. 43. In general, we attempted to heed the admonitions of Godyak.<sup>45</sup> Briefly, the probe was a 2.9 mm long, 0.63 mm diam wire supported by a 1.5 mm diam ceramic holder. Identical results were obtained with nickel-chrome and with platinum wires. The probe wire was connected to a pulser through a tuned resonant circuit that insured that the probe had high impedance at 13.56 MHz. The probe was held at 20–40 V negative bias by a dc supply and was pulsed positive by triangular pulses with durations of approximately 1 ms and repetition rate of 10 Hz. The potential-current characteristics were recorded and averaged during the triangular pulses by a high-speed digitizer. The short pulse and low duty cycle insured that the probe surface did not change during the data-acquisition cycle. Use of slower pulses (50 ms duration) showed hysteresis, i.e., different characteristics during the rise and fall of the pulses. This suggested that probe surface conditions were changing rapidly, even in argon discharges. Consequently, the short pulse seemed necessary. However, the high-speed digitizer had only an 8 bit resolution, and, thus, we could not resolve details of the distribution function with a single digitizer. The dc component of the plasma potential, denoted as  $V_p0$ ,

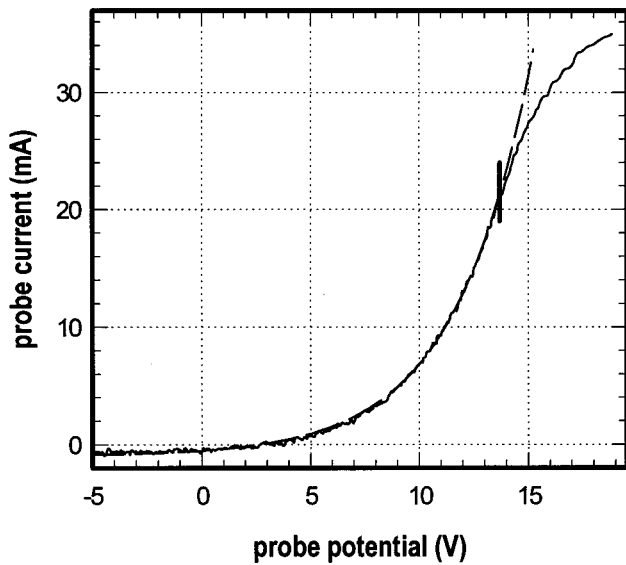


FIG. 8. Sample Langmuir-probe characteristics with the probe near the corner of the discharge region at the scan-1 elevation (Fig. 4). The vertical bar marks the plasma potential as determined from second-derivative analysis. The dashed line is a Maxwellian fit to the data with parameters  $n_e = 1.1 \times 10^{11}/\text{cm}^3$ ,  $T_e = 3.5$  eV, and  $V_p = 13.7$  eV.

was determined by finding the zero of the second derivative of a sliding polynomial that was fitted to the potential-current curve. The bulk electron temperature  $T_e$  was determined by fitting a straight line to the log-current versus-potential curve. The electron density was determined using  $T_e$  and the probe-current value at  $V_p$ . We employed standard probe theory for the limit where the Debye length is much shorter than the probe dimensions.

Previously,<sup>43</sup> we compared values of electron density determined with this probe technique against values determined by an 80 GHz microwave interferometer. In general, the interferometer is thought to be the more reliable technique. The comparison employed a series of four probes of different sizes. The comparison showed that, as the probe size was reduced, the values of the electron density given by the probe increased and approached the interferometer values from below. With the probe used in the present experiment (probe D in Ref. 43), the electron density determined with the probe was 20% lower than the interferometer value. Consequently, we applied an upward correction of 25% to the probe-measured electron densities to obtain densities expected to be present when the probe and its holder were not intruding into the plasma. A sample probe potential-current trace is shown in Fig. 8.

The sheath model given in Sec. II requires as input the value of the electron density and temperature at the “edge” of the bulk plasma, which is commonly taken to be the Bohm point. In the experiment with applied rf bias, it was not known precisely where to position the probe to obtain plasma “edge” parameters. Furthermore, as pointed out by Godyak,<sup>45</sup> probe theory assumes that the plasma has gradient scale lengths much longer than mean-free paths (for collisions, ionization, and energy relaxation). Consequently, even if the plasma edge location were known precisely, the probe

theory would not strictly apply because that location necessarily would involve very short gradient scale lengths. With all these problems in mind, we chose to use probe results taken with the probe located a practicable 5 mm away from the material surfaces (window, walls, lower electrode) as representing the “edge” of the plasma. This was close to being an ion mean-free path away from the surfaces. Results presented below, along with sensitivity studies, indicate that this choice was fairly successful.

### E. Capacitive probe

The Langmuir probe described above was used to measure the dc component of the plasma potential  $V_p0$ . A capacitive probe immersed in the plasma was used to measure the rf components  $V_p1$ ,  $V_p2$ , etc. In our notation,  $V_p1$  refers to the component at the fundamental frequency (13.56 MHz),  $V_p2$  to the second harmonic at 27.12 MHz, etc. The capacitive probe tip was a cylindrical piece of metal ( $<1$  cm<sup>2</sup> surface area) attached to the center conductor of a length of 50  $\Omega$  semirigid coaxial cable. This probe assembly was enclosed in 6 mm diam Pyrex tubing, which was positioned in the plasma using an  $x$ - $y$ - $z$  manipulator. The signal from the probe was recorded by oscilloscope with 50  $\Omega$  termination. The probe was calibrated by wrapping the tip of the tubing with aluminum foil, by exciting the foil with a calibration signal, and by comparing the excitation amplitude to the probe response.

The probe signal was proportional to the current through the Pyrex to the probe tip, which was the displacement current corresponding to the time derivative of the plasma potential. Consequently, the probe signal required integration to yield the plasma potential. This integration was performed in the frequency domain after performing a Fourier transform. Wave forms of the plasma potential were reconstructed by performing inverse transforms on the integrated data.

## VI. RESULTS AND DISCUSSION

This section presents the results of the experiment and comparisons to model calculations. First, the conditions of the bulk plasma are discussed, which set the boundary conditions for the sheath model. Second, the measured and computed electrical signals are compared.

### A. Bulk plasma parameters

Plasmas were formed in argon at 10 mTorr pressure with 250 W input at 13.56 MHz to the induction-coil circuit. Resistive losses in the circuit consumed approximately 20% of this power, leaving 200 W power deposited in the plasma. The total volume of the plasma region was approximately 900 cm<sup>3</sup> (Fig. 4) and, thus, the average specific power deposition was 0.22 W/cm<sup>3</sup>. Figure 9 shows radial profiles of  $n_e$ ,  $T_e$ , and  $V_p$  measured by the Langmuir probe at three different elevations in the plasma region denoted by scans 1–3 in Fig. 4. The electron density was clearly peaked radially in the center of the chamber and decreased toward the lower electrode (scan 3). Based on these profiles, it is probable that peak specific power deposition approached or exceeded 1 W/cm<sup>3</sup>. Figure 10 compares the electron density computed

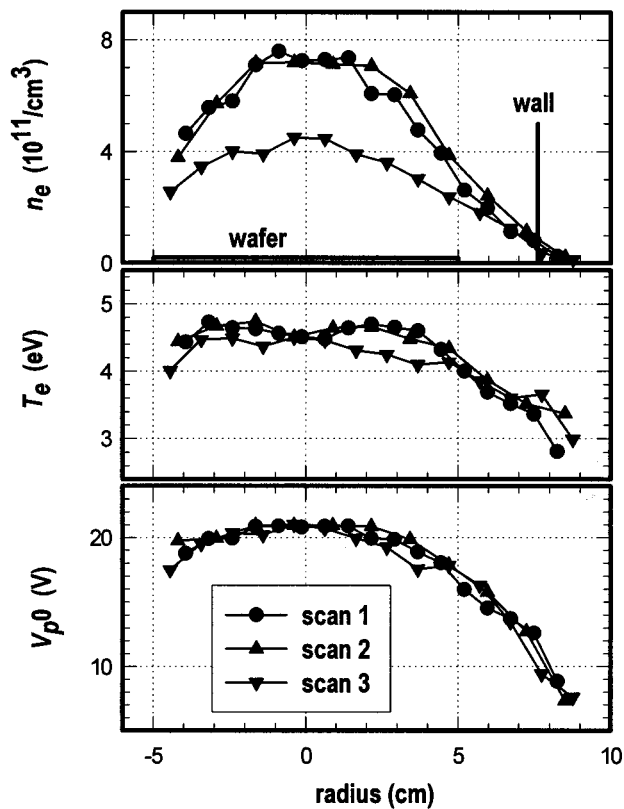


FIG. 9. Langmuir-probe data for a standard 250 W discharge in argon at 10 mTorr with no rf bias. The different probe scans were at different elevations, as shown in Fig. 4. The data show that the low-density plasma leaking through the diagnostic slot in the wall (containment can) was clearly detectable.

from the electron-collection characteristics of the Langmuir probe with the ion density computed from the ion saturation current. For the ion current measurements, the probe was biased at  $-20$  V with respect to the reactor walls, or ap-

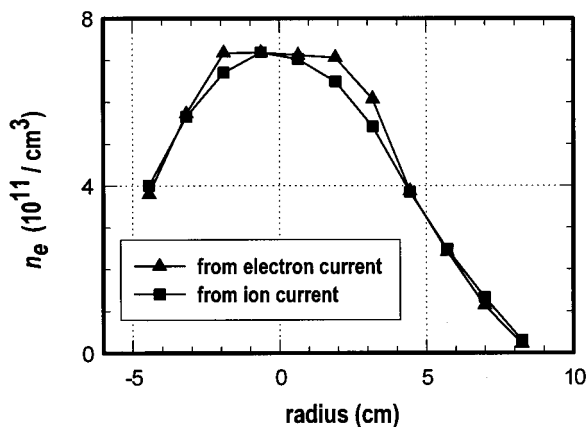


FIG. 10. Comparison of radial profiles of electron density, determined from the electron-collection characteristics of the Langmuir probe, and ion density, determined from the ion saturation current. The ion density has been computed from the ion saturation current density using the formula  $n = 0.692(J_{\text{sat}}/eu_B)$ , where  $T_e$  (radially dependent) was taken from the data in Fig. 9 to compute the Bohm velocity, and the leading numerical factor was selected to match the peak densities. The data are for the scan-2 elevation.

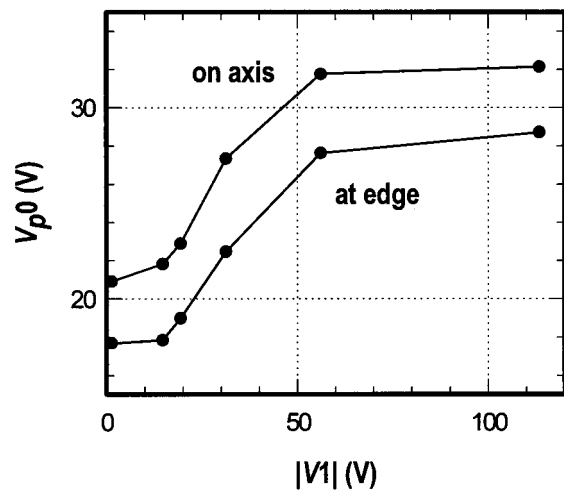


FIG. 11. Langmuir-probe measurements showing the variation with rf bias ( $V1$ ) of the dc component of the plasma potential ( $V_{p0}$ ). The measurements at the center ( $r=0$ ) and edge ( $r=5.5$  cm) of the discharge demonstrate that changes in  $V_{p0}$  with bias were spatially uniform. The probe was 17 mm above the wafer.

proximately  $-40$  V with respect to the plasma potential. The ion current density was computed from the probe current using the mechanical surface area of the probe tip. The radial shapes in Fig. 10 agree fairly well, but a numerical multiplier of 0.692 was needed to fit the absolute magnitudes of the central peaks. This deviation from Eq. (38) could be explained, for example, if the effective ion-collection area were 44% larger than the surface area of the cylindrical probe tip due to radial sheath expansion at large negative bias.

Figures 11 and 12 address the spatial variation of changes in the plasma potential due to rf bias applied to the lower electrode. As discussed in Sec. II, the bulk-plasma treatment assumed that the changes in both dc and rf components of the plasma potential due to applied rf bias were spatially uniform. Figure 11 shows the dc component of the plasma potential  $V_{p0}$  at the center and edge ( $r=5.5$  cm) of the discharge as measured by the Langmuir probe. The potentials are shown as functions of  $V1$ , the 13.56 MHz Fourier coefficient of the rf bias at the lower electrode. These data verify that the dc shift in plasma potential due to rf bias was *spatially uniform* even though the absolute value of the plasma potential had significant spatial gradients. These data also show that the change in the dc component of the plasma potential was not linear with rf bias. Figure 12 shows the spatial variations of magnitudes and phases of the 13.56 and 27.12 MHz components of the plasma potential as measured by the capacitive probe immersed in the plasma. These data, taken for  $|V1|=48$  V, verified that the rf components of the oscillating plasma potential were spatially uniform. The decline in potential near the wall was probably due to the size of the probe sense element, which was 1.1 cm long in the radial direction. For measurements near the wall, part of the sense element was close to the wall or inside the slot in the wall. Oscillations in the potential of the low-density plasma leaking through the diagnostic slot in the wall were clearly detectable to large radius.



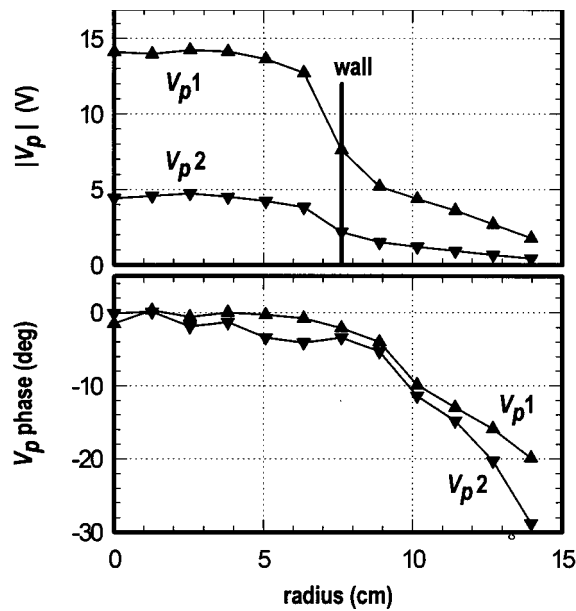


FIG. 12. Capacitive-probe measurements of the rf components (fundamental =  $V_{p1}$ , second harmonic =  $V_{p2}$ ) of the plasma potential vs radius with applied rf-bias  $|V_1| = 48$  V. The phase measurements are relative; for this plot the maximum phase was set to  $0^\circ$ . These measurements show that the oscillating components of  $V_p$  were spatially uniform. The decrease in amplitude near the wall (containment can) was affected by the length of the capacitive-probe tip (1.1 cm). Oscillations in the low-density plasma leaking through the slot in the containment can were clearly detectable.

Note that the spatial uniformity of the perturbations in the plasma potential caused by the applied rf bias implied that the rf-bias power was not being deposited in the bulk plasma by resistive dissipation in the bulk. This is in keeping with the overall intent of high-density plasma reactors, which is to decouple the plasma generation process from the ion extraction process. This decoupling allowed us to use bias powers up to 150 W without significantly affecting the properties of the bulk plasma that was generated by the 250 W induction source. Indeed, Langmuir probe measurements showed no significant change in electron density at the center or edge of the plasma when rf bias (up to 125 W) was applied to the lower electrode.

## B. Comparison between measured and computed potentials and currents

Harmonic analysis of the measured voltage and current at the rf-biased lower electrode was performed as described above in Sec. IV B. Computations iterated a set of differential equations that embodied the circuit of Fig. 2 with the sheath model of Sec. III, which can be summarized by Eqs. (44)–(52). Comparisons of wave forms as well as comparisons of Fourier-expansion coefficients are presented in this section.

Comparisons between calculated and measured wave forms are presented in Fig. 13 for a representative case where the rf bias was  $|V_1| = 113$  V. For these computations, the rf voltage source in Fig. 2 was adjusted until the computed  $V_1$  equaled the measured value. Figure 13 presents

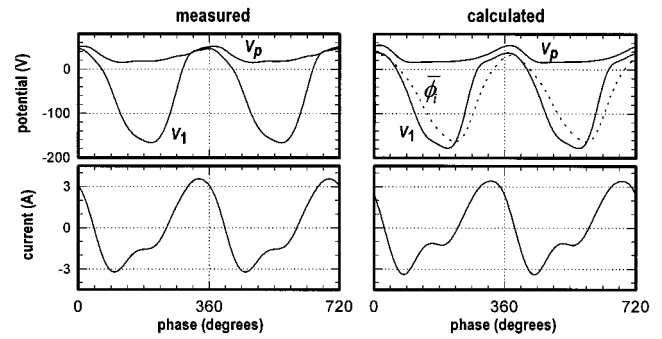


FIG. 13. Comparison of calculated and measured wave forms of electrode potential  $V_1$ , plasma potential  $V_p$ , and electrode current  $I$ . The wave forms were constructed from six harmonics of the Fourier-analyzed measurements and the computed solutions to the differential equations. The data and computations were for  $|V_1| = 113$  V. The time axes were adjusted so that the phase of  $V_1$  was  $0^\circ$ . The dotted line is the calculated synthetic potential  $\bar{\phi}_i$ , which described ion motion. The instantaneous ion energy in the model was the difference between  $V_p$  and  $\bar{\phi}_i$ , plus  $kT_e/2$ , as may be seen in Eq. (26).

two cycles of wave forms for electrode potential, plasma potential, and electrode current. There are several features of note for the case presented in Fig. 13:

- (1) The magnitudes of the measured and calculated currents are in excellent agreement, as is the general nature of the distortion that occurred just after the negative peak in the current. Recall that the current computations depended only on *measured* plasma and circuit parameters; there were no arbitrary adjustable parameters in the model.
- (2) The magnitudes and shapes of the plasma potentials are in excellent agreement.
- (3) The shapes of the negative peaks in the potential wave forms are quite similar.
- (4) Close examination shows that there is more phase difference between the calculated electrode potential and current than between the measured electrode potential and current. The larger phase difference in the calculations indicates lower calculated power than measured power. (This difference is quantified below.)
- (5) There is disagreement between the measured and computed differences between the electrode potentials and the plasma potentials. In the calculations, there was a nearly constant difference of approximately 20 V for nearly  $135^\circ$  of the cycle near the positive peak in the potential. In contrast, the experiment found that the difference vanished for more than  $45^\circ$ . During this part of the cycle, electrons in the tail of the distribution function are supposed to be flowing to the electrode in sufficient quantity to compensate for the constant flow of ion saturation current to the electrode.
- (6) The time behavior of the potential  $\bar{\phi}_i$  indicated that the low-frequency limit of MEO<sup>19</sup> would be a better description for *this case* than the high-frequency limit of Lieberman.<sup>18</sup>

The disagreement between model and experiment about the difference between plasma and electrode potentials [item (5) above] could have several sources. If the disagreement were a real phenomenon, it would imply that the experimen-

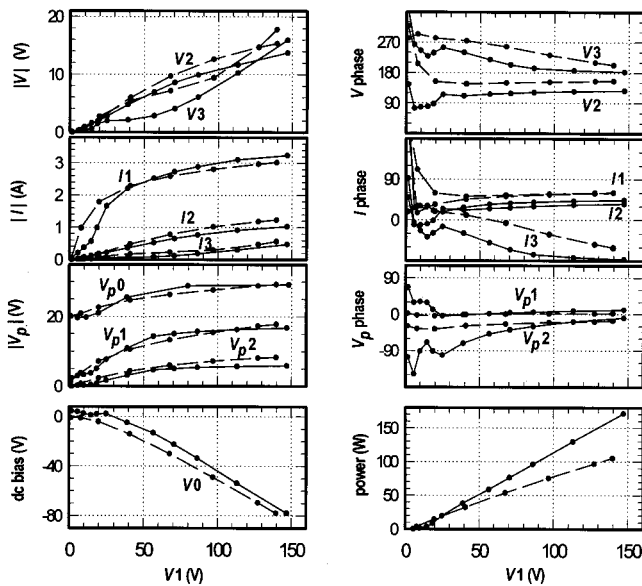


FIG. 14. Comparison of calculated and measured Fourier coefficients of potential and current at lower-electrode, plasma-potential, dc-bias, and rf-bias power. The independent variable is  $V_1$ , the 13.56 MHz component of the electrode potential, whose phase was defined as  $0^\circ$ . The solid lines are measured values and the dashed lines are calculated values. The phase values are given in degrees. The text clarifies assignments of magnitudes of  $V_2$  and  $V_3$  and phases of  $I_1$  and  $I_2$ .

tal electron distribution function was very strongly non-Maxwellian during this part of the cycle, which would violate a basic assumption of the sheath model. In order for the electron current to the electrode to be comparable to the ion current and much less than the electron saturation current, the tail would need to be extremely depleted during this part of the cycle. It seems more likely to us that an experimental measurement error in potential magnitude and/or phase was the source of the discrepancy. The potential difference was the result of subtracting two potentials measured by very different techniques: one used combined results from Langmuir and capacitive probes in the plasma while the other used potential and current probes in the electrode circuit and employed a circuit model for interpretation. If the amplitude of the measured rf electrode potential were in error by  $+10\%$  as a result of errors in calibration or in the circuit model, then the actual experimental voltage difference would be in substantial agreement with the model. Alternatively, if there were a  $+20^\circ$  phase error in the electrode potential measurement, then the measured difference would not vanish and the relative phasing of the electrode potential and current would be closer to the model phasing.

Figure 14 shows the results of measurements and calculations for a wide range of applied rf bias. For all the graphs, the independent variable is the magnitude of  $V_1$ , whose phase was defined as  $0^\circ$ . Figure 14 shows magnitudes and phases of three Fourier-expansion coefficients for the lower electrode potential ( $V_0$ ,  $V_2$ ,  $V_3$ ), the lower electrode current ( $I_1$ ,  $I_2$ ,  $I_3$ ), and the plasma potential ( $V_{p0}$ ,  $V_{p1}$ ,  $V_{p2}$ ). Also shown is the rf-bias power. In all cases, the measurements are denoted by solid curves and the calculations by dashed curves. The curve labels were placed as close as possible to

the corresponding curves. Note that the magnitude curves for  $V_2$  are concave down while the curves for  $V_3$  are concave up. Also note that the calculated curves for the phases of  $I_1$  and  $I_2$  were indistinguishable from each other at higher bias powers, while the measured phase of  $I_1$  was above (higher) than the phase of  $I_2$ .

There are several features to note in Fig. 14:

- (1) The magnitudes of the measured and calculated currents and plasma potentials are in excellent agreement except at the lowest values of  $V_1$ .
- (2) The magnitudes of measured and calculated  $V_0$  (dc bias) and  $V_2$  are in good agreement; there is fair agreement in  $V_3$ .
- (3) The measured and calculated phases have the same asymptotic shapes at high  $V_1$ , but there is a consistent positive phase difference in the values of the phase of the electrode potentials and currents.
- (4) There is poor agreement in the phases at low applied rf bias where the capacitive current from the induction coil was dominant.
- (5) The measured rf power is significantly below the calculated power.

Overall, we are very pleased with the degree of agreement achieved between the model and experiment, as shown in Figs. 13 and 14. Nevertheless, we have considered several possible factors that might contribute to the discrepancies. Of course, approximations in the models (e.g., treatments of ion inertia and secondary electrons) may contribute to the discrepancies, but these effects are difficult to investigate directly. Regarding item (3) above, our measurement technique should maintain better phase accuracy between the potential and current of a single harmonic than between different harmonics. This is seen in the results, for example, by noting that the phase differences measured between  $V_3$  and  $I_3$  are in good agreement with the phase differences calculated between  $V_3$  and  $I_3$ . Similarly for  $V_2$  and  $I_2$ . The experimental phase errors described by Fig. 6 contribute to the discrepancy in item (3), but do not seem nearly as large as the phase differences in Fig. 14. Regarding item (4) above, the large phase discrepancies at low bias in Fig. 14 we attribute to an error in our treatment of the capacitive currents flowing through the induction window. Either the phase measurements of the current coupled into the plasma from the coil were in error or the impedance for currents flowing out from the plasma was incorrect in the model. Such errors would strongly affect the low-bias data, where the currents capacitively coupled through the induction window were greater than the lower-electrode currents.

The model assumed that the lower electrode was a perfect electric conductor, while in the experiment we covered the metal electrode with a 10 cm diam silicon wafer to prevent sputtering of metal onto the coupling window. The skin depth for rf signals was not thin compared to the wafer thickness, and the wafer may have affected the phases of the signals in some way.<sup>44</sup> The quality of the electrical contact between the wafer and the electrode was unknown. Also, at low-bias levels there was minimal ion bombardment of the wafer, and an insulating native-oxide coating may have been

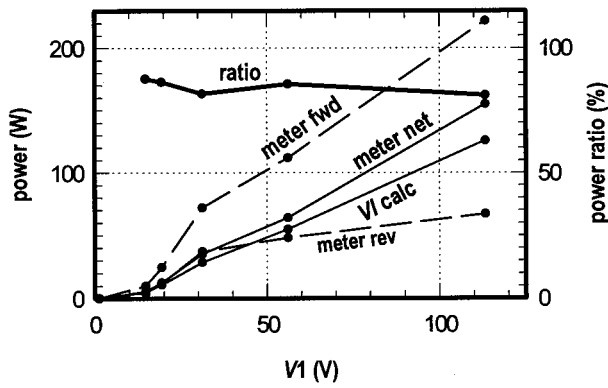


FIG. 15. Comparison of forward, reflected, and net bias power indicated by the analog watt meter, and the power computed from the product of the electrode potential and current ("VI calc"). For the electrical data, the phase difference between voltage and current ranged from  $19^\circ$  at low bias to  $44^\circ$  at high bias. Also shown by the heavy line is the ratio of the computed power to the net watt meter power. That ratio was  $84\% \pm 3\%$  for all the data, consistent with a modest power loss in the low-pass filter.

present and may have affected current flows. We have not quantified the possible effects on the data due to the wafer.

To investigate the discrepancy between measured and calculated power at the lower electrode, comparisons were made between the readings of an analog watt meter and the power computed from the measured rf potential and current. The watt meter was connected between the coaxial cable and the low-pass filter shown in Fig. 4. This location was desirable for watt meter accuracy because no harmonic signals reached the watt meter, but any power losses in the filter would cause a difference in the power at the watt meter and at the location of the electrical probes. Figure 15 shows power measurements over a range of bias levels. In all cases, the ratio of the power calculated from the electrical probe signals to the net watt meter power was  $84\% \pm 3\%$ . This is consistent with a moderate power loss in the filter of  $16\% \pm 3\%$ , which could have been caused by resistance in the two  $2\ \mu\text{H}$  coils in the filter. While this power measurement was not conclusive, it did *not* suggest the presence of major errors in the electrical magnitude and phase measurements at the fundamental frequency.

Another possible source of error in the model computations of phase and power could be the use of incorrect values of bulk-plasma parameters as boundary conditions for the sheath code. Recall that Langmuir-probe data obtained 5 mm from the walls were used to represent Bohm-point conditions. There was uncertainty as to the appropriateness of that distance from the walls for the Bohm point and there was uncertainty as to probe performance in the presence of strong gradients in the plasma parameters. To investigate the sensitivity of the model to these effects, a series of calculations was performed with various values of  $T_e$  and  $n_e$ . For these calculations,  $|V1|$  was maintained at 113 V, as in Fig. 13. Computed results were only weakly dependent on the assumed values of  $T_e$  over the range 2–7 eV. This weak dependence on  $T_e$  suggests that the model and experimental results would not be very sensitive to the shape of the electron energy distribution function. Depletion of the tail due to

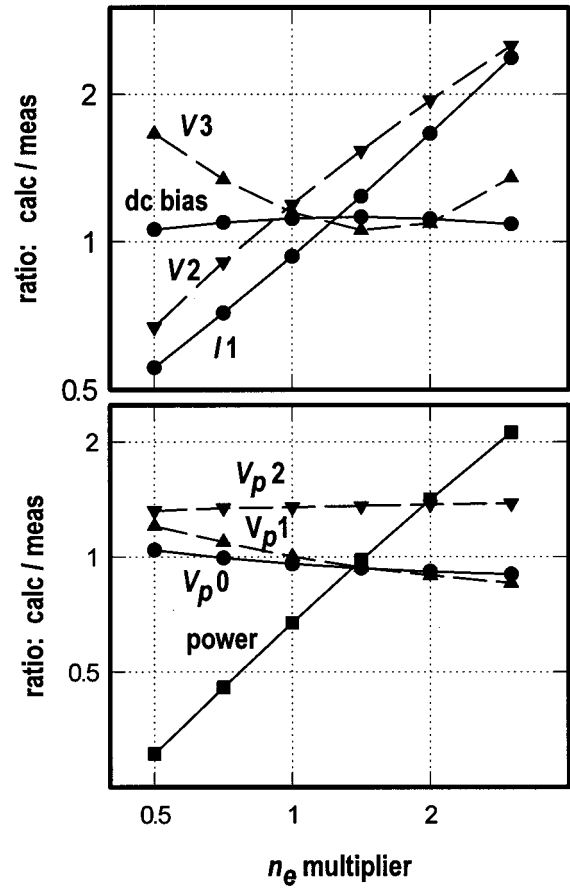


FIG. 16. Dependence of Fourier-coefficient magnitudes, dc bias, and power on the electron density assumed in the code calculations, for the case  $|V1| = 113\ \text{V}$ . The  $n_e$  multiplier is a factor that was used to raise or lower all the values of electron density in the calculations. Note the improved agreement in power for an electron density slightly higher than was obtained from the probe measurements. Note also how the model and experiment would disagree for electron densities a factor of 2 higher or lower than measured.

diffusion and inelastic collisions, or enhancement of the tail due to instabilities, would affect the difference between the plasma potential and the electrode and wall potentials, as mentioned above. But the effect on phase and power apparently is weak. In contrast, some computed values, including power, were strongly dependent on the assumed electron density. Figure 16 shows the magnitudes of several computed quantities as functions of the electron density. Two separate graphs are shown merely to make the different curves easier to identify. For each of these calculations, electron density values in all zones were multiplied by the single constant multiplier given on the abscissa. The ordinates are the ratios of the calculated quantities to those measured in the experiment.  $I2$  and  $I3$  are not shown because they are uniquely related to  $V2$  and  $V3$  by the circuit impedance, and thus, they necessarily provide only the same information that is present in  $V2$  and  $V3$ . It is evident that there would be better agreement in power if a higher value of electron density (25%–50% higher) were assumed in the calculations. This could be related to the position where the density was measured, see the discussion at the end of Sec. V D. Computed plasma potential values were not sensitive to electron density, in contrast to the current  $I1$  and the second har-

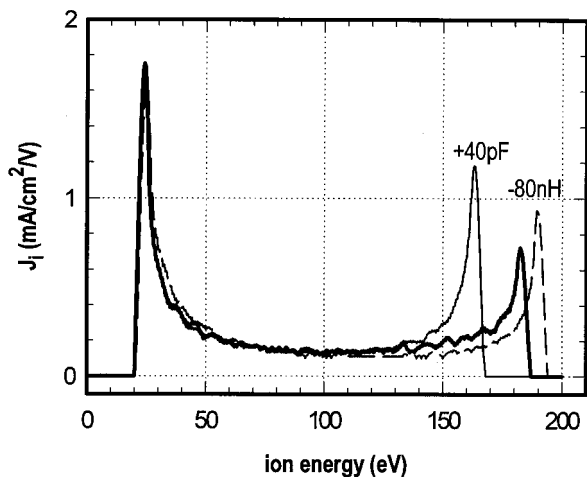


FIG. 17. Computed ion energy spectra showing that ion energies are not unique functions of rf power. The heavy curve accompanies the wave forms shown in Fig. 13. The other two curves are from calculations with powers identical to that of the heavy curve (87.3 W), but with changes made to the rf circuit components.

monic of voltage V2. The phases that accompanied the calculations of Fig. 16 still had substantial differences from the experiment.

The calculated results in Fig. 16 can be viewed as providing strong support for our modeling methodology. Note that, while the experimental results are not precisely replicated by the model, there would be much stronger disagreement if, for example, the electron density were changed by a factor of 2 in either direction. In our experience, this is rather good agreement between plasma-physics experiments and first-principles models.

## VII. ION SPECTRA

The sheath model computes the energy spectrum of ions crossing the sheath. Since the sheath is electrically nonlinear, it follows that the ion energy spectrum is not necessarily a unique function of any single electrical parameter in the circuit. To investigate this, calculations were performed keeping constant the rf power delivered to the sheath, while values of inductance and capacitance in the rf excitation circuit were varied. Figure 17 shows ion spectra for three sample cases, all at 87.3 W input power to the lower electrode. The heavy line is for the base-line case described by the wave forms in Fig. 13. Another case in Fig. 17 (lighter solid line) had an additional 40 pF capacitance added in parallel across the output of the low-pass filter shown in Figs. 2 and 5. The third case in Fig. 17 (dashed line) was the base-line case with an 80 nH reduction in the series inductance feeding power to the lower electrode. Table I shows Fourier components of the electrode voltage for these three cases, listed across in order of increasing peak ion energy. Detailed examination of these results shows that the computed peak ion energies do not vary linearly with any single voltage component. Also note that the peak ion energy does not vary monotonically with dc bias. There is no apparent “shortcut” to obtain accurate quantitative information about the ion spectrum; a complete analysis of the problem is required.

TABLE I. Dependence of peak ion energy and voltage components on circuit parameters.

	+ 40 pF	Base line	– 80 nH
Ion peak (eV)	163	182	188
Dc bias (V)	– 56.9	– 60.0	– 59.4
V1 (V)	106.8	113.0	120.3
V2 (V)	4.2	13.9	22.1
V3 (V)	11.6	11.7	0.5

These cases show that the computed high-energy part of the ion spectrum was sensitive to circuit values, even though the rf power was held constant. In an industrial reactor, such changes in ion spectrum would probably cause process shifts. Furthermore, a simple adjustment of bias power could not be used to eliminate the process shift because power changes would affect many parameters, not just the peak energy of the ions. Of course, further experimental work is needed to test these code predictions.

## VIII. SUMMARY

We have presented an analytic model for rf plasma sheaths that removes restrictions of previous sheath models concerning excitation frequency, harmonicity, and current flows. The model assumes a Boltzmann electron distribution function and assumes that cold ions traverse the plasma sheath, moving in a damped synthetic potential. The model is computationally efficient, and thus, is useful for inclusion as a boundary condition in comprehensive multidimensional plasma models that treat the physics and chemistry of the bulk plasma.

An experiment performed with an inductively coupled plasma reactor tested the sheath model’s accuracy in predicting the nonlinear relationship of potential and current at a rf-biased electrode in the plasma. The model was applied to the experiment without resorting to adjustable parameters. The experimental results agreed in detail with model predictions in most respects. This agreement is regarded as providing significant validation for the model. Relative phases of signals at different harmonic frequencies differed somewhat between the model and experiment, a result that may have had experimental causes.

Experimental measurements confirmed the postulated spatial uniformity of dc and rf modulation of the plasma potential caused by the applied rf bias on the capacitively coupled electrode. Experimental measurements also confirmed that the bulk plasma was not affected significantly by bias-power levels approaching the power consumed by the induction source to sustain the bulk plasma. This latter result would not necessarily occur in etching reactors because changes in rf bias would change etch rates and etch-product flows, which would change the gas mixture of the bulk plasma.

The various harmonics of voltage and current were found to be related in unique ways to bulk-plasma properties. For example, as shown in Fig. 16,  $I_1$  and V2 were both proportional to electron density for the particular conditions of this experiment. Similar relationships could be anticipated

in other systems, and the modeling methodologies presented here enable prediction and understanding of such relationships. These methodologies also enable design of rf electrical circuits to optimize signals. Thus, harmonic measurements could provide an inexpensive, nonperturbing diagnostic of plasma conditions that could be understood on the basis of the first-principles analysis embodied in the plasma-sheath model. This could be of value for control systems.

Ion energy distribution functions are predicted by the plasma model, but experimental verification of this important model feature remains to be performed. The model demonstrated sensitivity of the ion energy spectrum to values of circuit parameters as well as to rf power. This is an important contribution to the understanding of process shifts experienced in industry when modifications are made to rf circuits.

## ACKNOWLEDGMENTS

The authors are grateful for the able technical support of Ben P. Aragon and for numerous helpful technical discussions with Gregory A. Hebner, Joseph R. Woodworth, and Robert B. Campbell (Sandia). The authors appreciate suggestions from Lee A. Berry, Oak Ridge National Laboratory (ORNL), concerning the importance of the sheaths at the reactor walls and possible effects due to the wafer on the lower electrode. The authors also benefited from numerous interactions with Victoria Resta and Gil Yetter (SEMAT-ECH) and with Tony Moore (SEMATECH) and (ORNL). This work was supported by SEMATECH and by the United States Department of Energy under Contract No. DE-AC04-94AL85000. Sandia is a multiprogram laboratory operated by Sandia Corporation, a Lockheed Martin Company, for the United States Department of Energy.

- <sup>1</sup>John H. Keller, John C. Forster, and Michael S. Barnes, *J. Vac. Sci. Technol. A* **11**, 2487 (1993).
- <sup>2</sup>John H. Keller, 42nd Gaseous Electronics Conference, Palo Alto, CA (1989), Paper No. QA-5 (unpublished).
- <sup>3</sup>John H. Keller, Michael S. Barnes, and John C. Forster, 43rd Gaseous Electronics Conference, Champaign-Urbana, IL (1990), Paper No. NA-5 (unpublished).
- <sup>4</sup>James A. O'Neill, Michael S. Barnes, and John H. Keller, *J. Appl. Phys.* **73**, 1621 (1993).
- <sup>5</sup>J. Hopwood, *Plasma Sources Sci. Technol.* **1**, 109 (1992).
- <sup>6</sup>J. Hopwood, *Appl. Phys. Lett.* **62**, 940 (1993).
- <sup>7</sup>J. Hopwood, C. R. Guarnieri, S. J. Whitehair, and J. J. Cuomo, *J. Vac. Sci. Technol. A* **11**, 147 (1993).
- <sup>8</sup>J. Hopwood, C. R. Guarnieri, S. J. Whitehair, and J. J. Cuomo, *J. Vac. Sci. Technol. A* **11**, 152 (1993).
- <sup>9</sup>Michael S. Barnes, John C. Forster, and John H. Keller, *Appl. Phys. Lett.* **62**, 2662 (1993).
- <sup>10</sup>Peter L. G. Ventzek, Robert J. Hoekstra, and Mark J. Kushner, *J. Vac. Sci. Technol. B* **12**, 461 (1994).
- <sup>11</sup>Mark J. Kushner, Wenli Z. Collison, Michael J. Grapperhaus, John P. Holland, and Michael S. Barnes, *J. Appl. Phys.* **80**, 1337 (1996).
- <sup>12</sup>D. J. Economou, T. J. Bartel, R. S. Wise, and D. P. Lymberopoulos, *IEEE Trans. Plasma Sci.* **23**, 581 (1995).
- <sup>13</sup>J. D. Bukowski, D. B. Graves, and P. Vitello, *J. Appl. Phys.* **80**, 2614 (1996).
- <sup>14</sup>V. Vahedi, M. A. Lieberman, G. DiPeso, T. D. Rognlien, and D. Hewett, *J. Appl. Phys.* **78**, 1 (1995).
- <sup>15</sup>C. Lee and M. A. Lieberman, *J. Vac. Sci. Technol. A* **13**, 368 (1995).
- <sup>16</sup>E. Meeks and J. W. Shon, *IEEE Trans. Plasma Sci.* **23**, 539 (1995).
- <sup>17</sup>Michael J. Grapperhaus and Mark J. Kushner, *J. Appl. Phys.* **81**, 569 (1997).
- <sup>18</sup>M. A. Lieberman, *IEEE Trans. Plasma Sci.* **16**, 638 (1988).
- <sup>19</sup>A. Metzke, D. W. Ernie, and H. J. Oskam, *J. Appl. Phys.* **60**, 3081 (1986).
- <sup>20</sup>Merle E. Riley, "Unified Model of the rf Plasma Sheath," Sandia National Laboratories Technical Report No. SAND95-0775 UC-401, printed May 1995.
- <sup>21</sup>Merle E. Riley, "Unified Model of the rf Plasma Sheath Part II - Asymptotic Connection Formulae," Sandia National Laboratories Technical Report No. SAND96-1948 UC-401, printed August 1996.
- <sup>22</sup>F. F. Chen, *Introduction to Plasma Physics and Controlled Fusion*, Vol. 1 (Plenum, New York, 1988), p. 290-ff.
- <sup>23</sup>David Bohm, in *The Characteristics of Electrical Discharges in Magnetic Fields*, edited by A. Guthrie and R. K. Wakerling (McGraw-Hill, New York, 1949), Chap. 3.
- <sup>24</sup>Valery A. Godyak and Natalia Sternberg, *IEEE Trans. Plasma Sci.* **18**, 159 (1990).
- <sup>25</sup>Peter C. Stangeby, in *Physics of Plasma-Wall Interactions in Controlled Fusion*, edited by D. E. Post and R. Behrisch (Plenum, New York, 1986), pp. 41-97.
- <sup>26</sup>Earl W. McDaniel and Edward A. Mason, *The Mobility and Diffusion of Ions in Gases* (Wiley, New York, 1973), Chap. 5.
- <sup>27</sup>K.-U. Riemann, *J. Phys. D* **24**, 493 (1991).
- <sup>28</sup>M. S. Benilov, *J. Phys. D* **29**, 364 (1996).
- <sup>29</sup>H.-B. Valentini and F. Herrmann, *J. Phys. D* **29**, 1175 (1996).
- <sup>30</sup>Wolfgang Wasow, *Asymptotic Expansions for Ordinary Differential Equations* (Interscience, New York, 1965), Chap. 10.
- <sup>31</sup>K.-U. Riemann, *Phys. Fluids B* **4**, 2693 (1992).
- <sup>32</sup>V. A. Godyak, *Phys. Lett.* **89A**, 80 (1982). The numerical study in Ref. 21 suggests that  $E_1 \approx -(kT_e/e\lambda)\log_{10}(\epsilon^2)$  for the QSS case in terms of the smallness parameter defined in Eq. (12).
- <sup>33</sup>T. E. Nitschke and D. B. Graves, *IEEE Trans. Plasma Sci.* **23**, 717 (1995).
- <sup>34</sup>Paul A. Miller and K. E. Greenberg, *Appl. Phys. Lett.* **60**, 2859 (1992).
- <sup>35</sup>Paul A. Miller, Louis A. Romero, and Paul D. Pochan, *Phys. Rev. Lett.* **71**, 863 (1993).
- <sup>36</sup>Paul A. Miller, *Proc. SPIE* **1594**, 179 (1992).
- <sup>37</sup>Paul A. Miller, Harold Anderson, and Michael P. Splichal, *J. Appl. Phys.* **71**, 1171 (1992).
- <sup>38</sup>Those components in the model were not shielded from signals below the operating frequency. Consequently, they did affect subharmonic generation, which occurred in the model at somewhat higher excitation levels than were tested in the experiment.
- <sup>39</sup>The authors are willing to share the source code in FORTRAN that solves a sample tutorial sheath and circuit problem, and the source code in C++ that was used for the comparison with the experimental results.
- <sup>40</sup>P. J. Hargis, Jr., K. E. Greenberg, P. A. Miller, J. B. Gerardo, J. R. Torczynski, M. E. Riley, G. A. Hebner, J. R. Roberts, J. K. Olthoff, J. R. Whetstone, R. J. Van Brunt, M. A. Sobolewski, H. M. Anderson, M. P. Splichal, J. L. Mock, P. Bletzinger, A. Garscadden, R. A. Gottscho, G. Selwyn, M. Dalvie, J. E. Heidenreich, Jeffery W. Butterbaugh, M. L. Brake, M. L. Passow, J. Pender, A. Lujan, M. E. Elta, D. B. Graves, H. H. Sawin, M. J. Kushner, J. T. Verdeyen, R. Horwath, and T. R. Turner, *Rev. Sci. Instrum.* **65**, 140 (1994).
- <sup>41</sup>Mark A. Sobolewski, *J. Vac. Sci. Technol. A* **10**, 3550 (1992).
- <sup>42</sup>William H. Press and Saul A. Teukolsky, *Comput. Phys.* **5**, 426 (1991).
- <sup>43</sup>Paul A. Miller, Gregory A. Hebner, Kenneth E. Greenberg, Paul D. Pochan, and Ben P. Aragon, *J. Res. Natl. Inst. Stand. Technol.* **100**, 427 (1995).
- <sup>44</sup>This was first pointed out to us by Lee A. Berry, Oak Ridge National Laboratory (private communication).
- <sup>45</sup>V. A. Godyak, in *Plasma-Surface Interactions and Processing of Materials*, edited by Orlando Auciello, Alberto Gras-Marti, Jose Antonia Valles-Abarca, and Daniel J. Flamm, NATO ADI Series E: Appl. Sci. **176**, 95 (1990).

Journal of Applied Physics is copyrighted by AIP Publishing LLC (AIP). Reuse of AIP content is subject to the terms at: <http://scitation.aip.org/termsconditions>. For more information, see <http://publishing.aip.org/authors/rights-and-permissions>.